

A 3 + 1 Computational Scheme for Dynamic Spherically Symmetric Black Hole Spacetimes – I: Initial Data

Jonathan Thornburg*

*Department of Physics and Astronomy, University of British Columbia
Vancouver, British Columbia, V6T 1Z1, Canada*

(July 30, 2018)

Abstract

This is the first in a series of papers describing a 3 + 1 computational scheme for the numerical simulation of dynamic spherically symmetric black hole spacetimes. In this paper we discuss the construction of dynamic black hole initial data slices using York’s conformal-decomposition algorithm in its most general form, where no restrictions are placed on K (the trace of the extrinsic curvature) and hence the full 4-vector nonlinear York equations must be solved numerically.

To construct an initial data slice, we begin with a known black hole slice (e.g. a slice of Schwarzschild or Kerr spacetime), perturb this via some Ansatz (e.g. the addition of a suitable Gaussian to one of the coordinate components of the 3-metric, extrinsic curvature, or matter field variables), apply the York decomposition (using a further Ansatz for the inner boundary conditions) to project the perturbed field variables back into the constraint hypersurface, and finally optionally apply a numerical 3-coordinate transformation to restore any desired form for the spatial coordinates (e.g. an areal radial coordinate).

In comparison to other initial data algorithms, the key advantage of this algorithm is its flexibility: K is unrestricted, allowing the use of whatever slicing is most suitable for (say) a time evolution. This algorithm also offers great flexibility in controlling the physical content of the initial data, while placing no restrictions on the type of matter fields, or on spacetime’s symmetries or lack thereof.

We have implemented this algorithm for the spherically symmetric scalar field system. We present numerical results for a number of asymptotically

*Address for correspondence: $t \leq 1998$ Aug 31 \Rightarrow Box 8–7, Thetis Island, British Columbia, V0R 2Y0, Canada, E-mail thornbur@theory.physics.ubc.ca; $t \geq 1998$ Sept 1 \Rightarrow Institut für Theoretische Physik, Universität Wien, Boltzmannngasse 5, A-1090 Wien, Austria

flat Eddington-Finkelstein-like initial data slices containing black holes surrounded by scalar field shells, the latter with masses ranging from as low as 0.17 to as high as 17 times the black hole mass. In all cases we find that the computed slices are very accurate: Using 4th order finite differencing on smoothly nonuniform grids with resolutions of $\Delta r/r \approx 0.02$ (0.01) near the perturbations, and Gaussian perturbations yielding scalar field shells with relative width $\sigma/r \approx \frac{1}{6}$ and with about 2/3 the black hole mass, the numerically computed energy and momentum constraints for the final slices are $\lesssim 10^{-8}$ (10^{-9}) and $\lesssim 10^{-9}$ (10^{-10}) in magnitude respectively. For similarly perturbed numerically computed “warped” vacuum slices, the Misner-Sharp mass function is independent of position, and the 4-Riemann quadratic curvature invariant $R_{abcd}R^{abcd}$ is equal to its (position-dependent) Schwarzschild-spacetime value, to within relative errors of $\lesssim 10^{-5}$ (5×10^{-7}) and $\lesssim 3 \times 10^{-4}$ (5×10^{-5}) respectively. All these errors show the expected $O((\Delta r)^4)$ scaling with grid resolution Δr .

Finally, we briefly discuss the errors incurred when interpolating data from one grid to another, as in numerical coordinate transformation or horizon finding. We show that for the usual moving-local-interpolation schemes, even for smooth functions the interpolation error is *not smooth*. If interpolated data is to be differentiated, we argue that either the interpolation order should be raised to compensate for the non-smoothness, or explicitly smoothness-preserving interpolation schemes should be used.

04.25.Dm, 02.70.Bf, 02.60.Lj, 02.60.Ed, 04.40.Nr

I. INTRODUCTION

Dynamic black hole spacetimes are interesting both astrophysically (e.g. in the study of supernova core collapse, active-galactic-nuclei engines, and binary neutron-star or black-hole decay and coalescence) and as laboratories in which to study the physics of strong-field gravitation itself (e.g. horizons, causality, cosmic censorship, and self-similarity). Such systems are time-dependent, strongly relativistic, and often highly asymmetric, and so are hard to study in detail except by numerical methods.

This is the first in a series of papers describing a $3 + 1$ computational scheme for the numerical simulation of dynamic black hole spacetimes. We discuss both our general computational scheme (which should be applicable to a wide range of dynamic black hole spacetimes), and its application to a specific test system, that of an asymptotically flat spherically symmetric spacetime containing a black hole surrounded by a (massless, minimally coupled) scalar field.¹ Accordingly, we first work out our formalism and describe our algorithms in generic terms (making no assumptions about spacetime symmetries or what types of matter fields may be present), and only then specialize first to the scalar field system, and finally to the spherically symmetric scalar field system.

In this paper we focus on the “initial data problem” of constructing suitable initial data on a Cauchy surface.² That is, we consider the problem of computing the 3-metric and extrinsic curvature for an initial data slice, such that the constraints are satisfied and the slice has a desired physical content.

For black hole spacetimes, we have the additional problem of dealing with singularities. Traditionally this has been done using freezing slicings (see, for example, Smarr (1984); Shapiro and Teukolsky (1986)), but more recently attention has focused on the “black hole exclusion” or “horizon boundary condition” technique³ (see, for example, Thornburg (1985, 1987, 1991); Seidel and Suen (1992); Thornburg (1993); Scheel *et al.* (1995a); Anninos *et al.* (1995); Scheel *et al.* (1995b); Marsa (1995); Marsa and Choptuik (1996); Scheel *et al.* (1997)), where the slices penetrate the event horizon and meet the singularity or singularities, but in each slice the computational domain (numerical grid) excludes or omits roughly the

¹We have previously (Thornburg (1993)) applied a similar computational scheme to a different test system, that of an asymptotically flat axisymmetric vacuum spacetime containing a black hole surrounded by gravitational radiation. Unfortunately, for that system we have been unable to obtain time evolutions free of finite differencing instabilities.

²The term “initial value problem” is sometimes used here. We find this terminology undesirable because it conflicts with standard usage elsewhere (e.g. in the study of differential equations, and indeed in this journal’s own Physics and Astronomy Classification Scheme), where it refers to the evolution of initial data, i.e. the time integration of a set of ODEs or PDEs given values of the state variables at some initial time.

³We prefer the former term as focusing attention on the underlying process – the exclusion of the black hole from the computational domain – rather than on the particular boundary condition used to implement it.

black hole region. (The precise region excluded varies between different black-hole–exclusion computational schemes.)

The black hole exclusion technique requires special consideration when constructing initial data, because the boundary of the excluded region becomes a new “inner” boundary for the computational domain, typically on or just inside the (each) black hole’s outermost apparent horizon.⁴ This new boundary requires corresponding boundary conditions for the (elliptic) constraint equations.

Because the computational domain includes the (event) horizon, the black hole exclusion technique requires that the slicing and the 3 + 1 field variables all be nonsingular and smooth there, and in fact throughout some neighbourhood of the horizon. This generally rules out maximal slices such as the Schwarzschild (Boyer-Lindquist) slices in Schwarzschild (Kerr) spacetimes; Eddington-Finkelstein (Kerr) or similar slices are usually used instead. For our purposes, the key property of these latter slices is that they have K , the trace of the extrinsic curvature, nonzero and spatially variable over most or all of the slices.

Our slices having generic K has an important impact on the initial data construction itself: York’s conformal-decomposition technique is widely used for solving the initial data problem, and we use it here, but historically it’s usually been used in one of several special cases in which the York equations simplify greatly. However, as discussed in section IV, none of these special cases apply for slices with generic K , so we must (numerically) solve the York equations in their full form.

In the remainder of this paper, we first summarize our notation (section II), then discuss the York conformal decomposition, its various special cases, our general methods for solving its equations, and its outer boundary conditions (sections III–VI). We then describe our Ansätze for choosing the inputs to and the inner boundary conditions for the York decomposition (section VII). We next describe our diagnostics for assessing the accuracy of our initial data and studying its physical content (section VIII), introduce our spherically-symmetric-scalar-field test system (section IX), describe our numerical methods (section X), and present some sample results from a numerical code incorporating these techniques (section XI). We end the main body of the paper with some conclusions and directions for further research (section XII). In the appendices we tabulate some of the 3 + 1 field variables for an Eddington-Finkelstein slice of Schwarzschild spacetime (appendix A), tabulate the detailed equations for our spherically-symmetric-scalar-field test system (appendix B), discuss the derivation of our 3 + 1 form of the Misner-Sharp mass function (appendix C), describe our numerical-coordinate-transformation algorithm (appendix D), describe our methods for quantitatively testing finite differencing convergence (appendix E), and discuss the non-smoothness of errors when interpolating data from one grid to another (appendix F).

⁴As discussed elsewhere (Thornburg (1993, 1998)), our particular form of the black hole exclusion technique currently places the inner boundary considerably inside the apparent horizon (typically at $\sim 75\%$ of the horizon radius), but the details of this are unimportant here.

II. NOTATION

We generally follow the sign and notation conventions of Misner *et al.* (1973), with a $(-, +, +, +)$ spacetime metric signature, $G = c = 1$ units, and all masses and coordinate distances also taken as dimensionless. We assume the usual Einstein summation convention for all repeated indices, and we use the Penrose abstract-index notation, as described by (e.g.) Wald (1984). However, for pedagogical convenience we often blur the distinction between a tensor as an abstract geometrical object and the vector or matrix of a tensor’s coordinate components.

We use the standard 3 + 1 formalism of Arnowitt *et al.* (1962) (see York (1979, 1983) for recent reviews). For our spherically-symmetric–scalar-field test system, we use coordinates (t, r, θ, ϕ) , with θ and ϕ the usual spherical-symmetry coordinates. However, we leave t and r arbitrary, i.e. we make no assumptions about the choice of the lapse function or (the radial component of) the shift vector.

The distinction between 3- and 4-tensors is usually clear from context, but where ambiguity might arise we use prefixes ⁽³⁾ and ⁽⁴⁾ respectively, as in ⁽³⁾ R and ⁽⁴⁾ R . Any tensor without a prefix is by default a 3-tensor. \mathcal{L}_v denotes the Lie derivative operator along the 4-vector field v^a . δ^i_j is the usual Kronecker delta.

We use $abcd$ for spacetime (4-) indices, and ∂_a denotes the spacetime coordinate partial derivative operator $\partial/\partial x^a$. g_{ab} denotes the spacetime metric and ∇_a the associated 4-covariant derivative operator.

We use $ijkl$ for spatial (3-) indices. ∂_i denotes the spatial coordinate partial derivative operator $\partial/\partial x^i$. g_{ij} denotes the 3-metric of a slice, ∇_i the associated 3-covariant derivative operator, and g the determinant of the matrix of g_{ij} ’s coordinate components. α and β^i denote the 3 + 1 lapse function and shift vector respectively. n^a denotes the (timelike) future pointing unit normal to the slices. $K_{ij} \equiv \frac{1}{2}\mathcal{L}_n g_{ij} \equiv -\nabla_i n_j$ denotes the 3-extrinsic curvature of a slice, and $K \equiv K_i^i$ its trace. $\rho \equiv n^a n^b T_{ab}$ and $j^i \equiv -n_a T^{ai}$ denote the locally measured energy and 3-momentum densities respectively. T_{ij} denotes the spatial stress-energy tensor, and $T = T_i^i$ its trace.

The 3 + 1 energy and momentum constraints are thus

$$C \equiv \left(R - K_{ij}K^{ij} + K^2 \right) - \left(16\pi\rho \right) = 0 \quad (1a)$$

$$C^i \equiv \left(\nabla_j K^{ij} - \nabla^i K \right) - \left(8\pi j^i \right) = 0 \quad (1b)$$

respectively, where R denotes the 3-Ricci scalar computed from g_{ij} in the usual manner.

$\text{diag}[\dots]$ denotes the diagonal matrix with the specified diagonal elements. $\text{Gaussian}(x=A, \sigma=B)$ denotes the Gaussian function $\exp(-\frac{1}{2}z^2)$, where $z \equiv (x - A)/B$.

III. THE YORK DECOMPOSITION

York (1971, 1972, 1973); Ó Murchadha and York (1974a, 1974b) have given an elegant theoretical analysis of the 3+1 initial data problem, which both clarifies its physical meaning and supplies a practical algorithm for its solution. (Isenberg (1979) also discusses several related topics related to the canonical formulation of gravity.) This “conformal decomposition”

approach to the initial data problem is reviewed by York (1979, 1983, 1985); York and Piran (1982). Choptuik (1982) also gives a very clear presentation of the York decomposition.

For present purposes, we view the York decomposition as defining a projection operator \mathcal{Y} which projects the field variables into the constraint hypersurface. In detail, \mathcal{Y} is defined as follows:

Given an initial (“base”) 3-metric g_{ij} , extrinsic curvature K_{ij} , and energy and 3-momentum densities ρ and j^i , we first split g_{ij} into its determinant g and the conformal metric $h_{ij} \equiv g^{-1/3}g_{ij}$, and K_{ij} into its trace K and the tracefree extrinsic curvature $E_{ij} \equiv K_{ij} - \frac{1}{3}g_{ij}K$. We then define the covariant derivative ∇_i and compute the 3-Ricci tensor and scalar R_{ij} and R , all using the base metric g_{ij} in the usual manner.

Next, we solve the nonlinear elliptic “York equation”

$$\nabla_i \nabla^i \Psi = \frac{1}{8}R\Psi + \frac{1}{12}K^2\Psi^5 - \frac{1}{8}F_{ij}F^{ij}\Psi^{-7} - 2\pi\rho\Psi^{-3} \quad (2a)$$

$$(\Delta_\ell \Omega)^i = \frac{2}{3}(\nabla^i K)\Psi^6 - \nabla_j E^{ij} + 8\pi j^i \quad (2b)$$

for the 4-vector⁵ $\mathbf{Y} \equiv (\Psi, \Omega^i)$, where $F^{ij} \equiv E^{ij} + (\ell\Omega)^{ij}$, and where the York “vector divergence” and “vector Laplacian” operators ℓ and Δ_ℓ are defined by

$$(\ell X)^{ij} = \nabla^i X^j + \nabla^j X^i - \frac{2}{3}g^{ij}\nabla_k X^k \quad (3a)$$

$$(\Delta_\ell X)^i = \nabla_j (\ell X)^{ij} \quad (3b)$$

$$= \nabla_j \nabla^j X^i + \frac{1}{3}\nabla^i \nabla_j X^j + R^i_j X^j \quad (3c)$$

for any (arbitrary) contravariant 3-vector X^i . We discuss boundary conditions for the York equation in sections VI and VII.

Finally, we define the output field variables $(g_{ij}, K_{ij}, \rho, j^i)_{\text{out}} \equiv \mathcal{Y}(g_{ij}, K_{ij}, \rho, j^i)$ by

$$(g_{ij})_{\text{out}} = \Psi^4 g_{ij} \quad (4a)$$

$$(K_{ij})_{\text{out}} = \Psi^{-2} F_{ij} + \frac{1}{3}K\Psi^4 g_{ij} \quad (4b)$$

$$(\rho)_{\text{out}} = \Psi^{-8} \rho \quad (4c)$$

$$(j^i)_{\text{out}} = \Psi^{-10} j^i \quad (4d)$$

Although it’s not obvious from the form of the equations, the output field variables determined in this way do indeed satisfy the constraints.

IV. SPECIAL CASES OF THE YORK DECOMPOSITION

As discussed by York (1979); Bowen and York (1980); York and Piran (1982); York (1983, 1989) and reviewed by Thornburg (1993), section A5.1, the York decomposition has several important special cases in which the general York equations (2) simplify considerably:

⁵Here and throughout our discussion of the York decomposition and equations, we use the term “4-vector” only in the sense of “4-tuple of real-valued functions”, not in the sense of “rank 1 4-tensor”.

- If the base field variables define a maximal slice ($K = 0$), or more generally if K is spatially constant, then the 4-vector nonlinear elliptic system (2) decouples into separate *linear* 3-vector (momentum) and nonlinear scalar (energy) constraint equations, which may be solved sequentially.
- If the base field variables define a slice which is both maximal and 3-conformally flat ($g_{ij} = \Phi^4 f_{ij}$ for some conformal factor Φ and flat 3-metric f_{ij}), the York equations simplify still further. In particular, for this case Bowen (1979b, 1979a); Bowen and York (1980); Bowen (1982) have found the (analytical) general solution for the (linear) momentum constraint equation (2b) subject to outer boundary conditions appropriate for an asymptotically flat spacetime. This means that only the (nonlinear) energy constraint equation (2a) need be solved numerically. Bowen (*op. cit.*) has also found several Ansätze for choosing the base extrinsic curvature K_{ij} in this case, such that the final field variables represent an initial slice containing a single black hole with freely specifiable mass, momentum, and spin. Since the momentum constraint equation (2b) is linear here, these base K_{ij} may be superimposed to obtain base K_{ij} values for multiple-black-hole slices. We discuss this case further below.
- If the base field variables define a slice which is time-symmetric ($K_{ij} = 0$) and 3-conformally flat, then the full 4-vector York equation (2) has a fully-analytical asymptotically flat solution, first explicitly found by Misner (1960), following an earlier suggestion of Einstein and Rosen (1935). The Misner solution, first studied numerically by Brill and Lindquist (1963), represents an arbitrary number of momentarily stationary “generalized Schwarzschild” black holes, each with freely specifiable “mass”.⁷

The special case where the initial slice is maximal and 3-conformally flat has been used in most past numerical work on the initial data problem. In particular, several authors, notably York and Piran (1982); Choptuik (1982); Dubal (1992), have used this technique to construct initial data slices containing single black holes with varying spins, surrounded by various amounts of gravitational radiation.

There have also been several extensions of this work to the multiple black hole case. Kulkarni *et al.* (1983); Kulkarni (1984b); York (1984); Bowen (1985) have used infinite series of “image charges” to construct a semianalytical solution for maximal 3-conformally flat base field variables satisfying “reflection symmetric” or “inversion symmetric” inner boundary conditions on the surfaces of each of N black holes, and Bowen and York (1980); Bowen *et al.* (1984); Kulkarni (1984a) have specialized this approach to the 2-black-hole case. Using these latter solutions, various authors, for example Rauber (1985, 1986); Cook (1990, 1991); Dubal *et al.* (1992); Cook *et al.* (1993); Matzner *et al.* (1998), have constructed a variety of numerical solutions for Ψ corresponding to initial data slices containing two black holes, each with freely specifiable⁶ “mass”, “momentum”, and “spin”.⁷ Thornburg (1985,

⁶The question of just what can and can’t be freely specified for these initial slices is somewhat subtle. York (1989) gives a brief discussion of this; see also Matzner *et al.* (1998).

⁷ “Mass”, “momentum”, and “spin” are in quotes here because (outside of spherical symmetry) these quantities aren’t uniquely defined for the individual black holes, unless they’re far enough

1987) has also constructed maximal 3-conformally-flat 2-black-hole numerical solutions for Ψ , but using an apparent horizon boundary condition (a version of the black hole exclusion technique) instead of reflection symmetry.

Oohara and Nakamura (1989) have used a modified version of Bowen’s analytical solution for Ω^i to construct initial data slices modeling a binary neutron star system. Because no black holes are present in this case, they avoided the problem of inner boundary conditions altogether.

As noted in the introduction, however, in this paper our concern is with initial slices where K is nonzero and spatially variable, so none of the special cases discussed in this section apply, i.e. we must solve the full 4-vector York equation (2) numerically.

V. SOLVING THE YORK EQUATIONS

The York equation (2) is a nonlinear elliptic PDE. To solve it, we first use a global Newton-Kantorovich “outer” iteration (Boyd (1989), appendix C), then use standard finite differencing methods to numerically solve each of the resulting sequence of “inner” linear elliptic PDEs.

In detail, we first rewrite the York equation (2) in the form

$$\mathbf{G}^0 \equiv \nabla_i \nabla^i \Psi - \frac{1}{8} R \Psi - \frac{1}{12} K^2 \Psi^5 + \frac{1}{8} F_{ij} F^{ij} \Psi^{-7} + 2\pi \rho \Psi^{-3} = 0 \quad (5a)$$

$$\mathbf{G}^i \equiv (\Delta_\ell \Omega)^i - \frac{2}{3} (\nabla^i K) \Psi^6 + \nabla_j E^{ij} - 8\pi j^i = 0 \quad (5b)$$

where we define $\mathbf{G} \equiv \mathcal{G}(\mathbf{Y})$ to be the left hand side 4-vector. We then linearize the continuum differential operator \mathcal{G} about the current continuum solution estimate \mathbf{Y} ,

$$\mathcal{G}(\mathbf{Y} + \delta\mathbf{Y}) = \mathcal{G}(\mathbf{Y}) + \mathbf{J}[\mathcal{G}(\mathbf{Y})](\delta\mathbf{Y}) + O(\|\delta\mathbf{Y}\|^2) \quad (6)$$

where $\delta\mathbf{Y}$ is a finite perturbation in \mathbf{Y} and the linear differential operator $\mathbf{J}[\mathcal{G}(\mathbf{Y})]$ is the linearization of the differential operator \mathcal{G} about the point \mathbf{Y} . We then neglect the higher-order (nonlinear) terms in (6) and solve for the perturbation $\delta\mathbf{Y}$ such that $\mathcal{G}(\mathbf{Y} + \delta\mathbf{Y}) = 0$. This gives the linear elliptic PDE

$$\mathbf{J}[\mathcal{G}(\mathbf{Y})](\delta\mathbf{Y}) = -\mathbf{G} \quad (7)$$

to be solved for $\delta\mathbf{Y}$. Finally, we update the approximate solution via $\mathbf{Y} \rightarrow \mathbf{Y} + \delta\mathbf{Y}$, and repeat the iteration until $\|\mathbf{G}\|$ is small.

It’s convenient to rewrite the definition (6) of the Jacobian operator \mathbf{J} in the differential form $d\mathbf{G} = \mathbf{J}(d\mathbf{Y})$ to more clearly express \mathbf{J} ’s physical meaning of mapping infinitesimal changes in \mathbf{Y} to infinitesimal changes in \mathbf{G} . With this interpretation in mind, it’s easy to see from (5) that the Jacobian is given by

$$d\mathbf{G}^0 = \nabla_i \nabla^i d\Psi - \frac{1}{8} R d\Psi - \frac{5}{12} K^2 \Psi^4 d\Psi - \frac{7}{8} F_{ij} F^{ij} \Psi^{-8} d\Psi + \frac{1}{4} F_{ij} \Psi^{-7} (\ell d\Omega)^{ij} - 6\pi \rho \Psi^{-4} d\Psi \quad (8a)$$

$$d\mathbf{G}^i = -4(\nabla^i K) \Psi^5 d\Psi + (\Delta_\ell d\Omega)^i \quad (8b)$$

apart to have separate approximate asymptotically flat regions.

Given a reasonable numerical solution of the updating equation (7) (discussed in section X), we find in practice that the Newton-Kantorovich iteration converges rapidly and robustly, typically reducing $\|\mathbf{G}\|_\infty$ to negligible levels (e.g. $< 10^{-10}$) in 3–5 iterations.

VI. OUTER BOUNDARY CONDITIONS

The York equation (2) is an elliptic PDE, and as such needs boundary conditions. Assuming the black hole exclusion technique, there are $N + 1$ boundaries for a slice with N black holes: an inner boundary near each black hole’s horizon, and an outer boundary near spatial infinity. We discuss the inner boundary conditions in section VII.

The outer boundary conditions are determined by the desired asymptotic forms of Ψ and Ω^i at spatial infinity. For an asymptotically flat spacetime, we have

$$\Psi = 1 \quad (\text{at spatial infinity}) \quad (9a)$$

$$\Omega^i = 0 \quad (\text{at spatial infinity}) \quad (9b)$$

Purely for the initial data computation (with no time evolution involved), one can treat the unbounded problem domain by compactifying, e.g. by introducing a new radial coordinate $s \equiv 1 - r_{\min}/r$. This has been done by, for example, Choptuik (1982); Rauber (1985, 1986).

However, if the initial data computation is being done in conjunction with a 3 + 1 time evolution code (as is our main interest here), it’s typically more convenient to not compactify the domain, but instead apply an approximate outer boundary condition at some finite outer boundary radius r_{\max} . When doing this, we can exploit the known asymptotic falloff of Ψ and Ω^i to obtain more accurate results than would be obtained by simply applying the spatial-infinity condition (9) at $r = r_{\max}$. As discussed by York (1979, 1980); York and Piran (1982); York (1983); Oohara and Nakamura (1989); York (1989); Cook (1990, 1991); Ó Murchadha (1992), this gives the Robin outer boundary conditions

$$(\nabla_k \Psi)n^k + \frac{\Psi - 1}{r} = O\left(\frac{1}{r^3}\right) \approx 0 \quad (\text{at } r = r_{\max}) \quad (10a)$$

$$n_j \left(\delta^i_k - \frac{1}{2}n^i n_k\right) (\ell\Omega)^{kj} + \frac{6}{7r} \left(\delta^i_k - \frac{1}{8}n^i n_k\right) \Omega^k = O\left(\frac{1}{r^3}\right) \approx 0 \quad (\text{at } r = r_{\max}) \quad (10b)$$

[In practice, one can often still obtain adequate accuracy by replacing the vector Robin condition (10b) by the simple (and tensorially incorrect) application of a scalar Robin condition (analogous to (10a)) separately to each coordinate component of Ω^i ,

$$(\nabla_k \Omega^i)n^k + \frac{\Omega^i}{r} = O\left(\frac{1}{r^3}\right) \approx 0 \quad (\text{at } r = r_{\max}) \quad (11)$$

We use this approximation in our numerical code, and find that it gives good results.]

[It’s also useful to note that for many coordinate conditions, the asymptotic forms of Ψ and Ω^i are identical in their leading terms to those for the 3 + 1 lapse function α and shift vector β^i (respectively). Hence for such coordinate conditions the boundary conditions for Ψ and Ω^i are also identical to those for α and β^i . In the context of a 3 + 1 code incorporating both initial data computation and time evolution, this may allow the same outer boundary condition code to be used for the York equation as for the coordinate conditions.]

VII. OUR INITIAL DATA ALGORITHM AND ANSÄTZE

Given the York projection operator, our overall initial data algorithm is as follows:

1. We begin with an exact (analytically known) black hole initial data slice, chosen according to some Ansatz. As discussed in sections I and IV, this will typically have K nonzero and spatially variable throughout the slice.
2. We apply an arbitrary (in general constraint-violating) perturbation, again chosen according to some Ansatz.
3. We apply the York decomposition to project the perturbed field variables back into the constraint hypersurface, solving the full 4-vector York equations numerically. Here the outer boundary conditions are dictated by the physics (cf. section VI), but an (another) Ansatz is needed to supply the inner boundary conditions.
4. Optionally, we apply a numerical 3-coordinate transformation to restore the spatial coordinates within the slice to some desired form, e.g. to make the radial coordinate areal ($g_{\theta\theta} = r^2$). We discuss numerical coordinate transformations in appendix D.

In comparison to other initial data algorithms, the key advantage of using the full York decomposition is its flexibility: Since no restriction is placed on K , almost any slicing may be used. That is, with this algorithm the slicing may be chosen based on its suitability for (say) a black-hole-excluded time evolution, rather than being limited by the initial data solver. As well, the physical content of the initial slice may be controlled over a wide range by varying the choices for the different Ansätze. This algorithm also places no restrictions on what type(s) of matter field(s) may be present, and (given suitable programming for the numerical solution of the York equations) it works equally well in spherical symmetry, in axisymmetry, or in fully generic spacetimes with no continuous symmetries.

To actually use this algorithm to construct initial data slices, we must make suitable choices for the various Ansätze. We now consider these choices:

As noted in the introduction, the black hole exclusion technique requires a slicing which penetrates the horizon, with the slicing and the $3 + 1$ field variables all nonsingular and smooth throughout some neighbourhood of the horizon. We thus use an Eddington-Finkelstein slice of Schwarzschild spacetime, or a Kerr slice of Kerr spacetime,⁸ for step 1 of our algorithm.

The choice of the perturbation Ansatz for step 2 of our algorithm is much less clear-cut, and we have experimented with a number of different choices for what field variable to perturb and what perturbation to apply. Provided the perturbation isn't too large, we have

⁸Recall that these slices are both defined (Misner *et al.* (1973), boxes 31.2 and 33.2) by taking the usual areal radial coordinate r , and defining t such that $t + r$ is an ingoing null coordinate. Both slices are nonsingular near to and on the horizon. For reference, in appendix A we tabulate some of the $3 + 1$ field variables for an Eddington-Finkelstein slice of Schwarzschild spacetime.

found that in practice essentially any smooth localized perturbation⁹ in the field variables “works”, in the sense that the York equations remain numerically well-behaved and yield a properly-constrained initial data set (still) containing a black hole. However, the precise relationship between the form of the perturbation and the nature of the resulting initial data slice is complicated and not (yet) easily predicted a priori. In section XI we present numerical results for several examples of this relationship (different choices of the perturbation), but much more research is needed to explore and map this relationship’s phenomenology.

To motivate the choice of an inner boundary condition Ansatz for the York equation (2) in step 3 of our algorithm, we first observe that if the base field variables already satisfy the constraints, then the York projection operator is the identity operator, i.e. the solution of the York equation (2) is $\Psi \equiv 1$ and $\Omega^i \equiv 0$. We then consider the slightly more general case where the base field variables are a small perturbation off the constraint hypersurface. To the extent that the perturbation is indeed small, or at least that its effects are small near the inner boundary, then $\Psi \equiv 1$ and $\Omega^i \equiv 0$ should still be an approximate solution of the York equation at the inner boundary. This suggests taking

$$\Psi = 1 \quad (\text{at the inner boundary}) \quad (12a)$$

$$\Omega^i = 0 \quad (\text{at the inner boundary}) \quad (12b)$$

as our inner boundary condition Ansatz for the York equation (2).

It’s not a priori obvious that (i) this boundary condition is consistent with any nontrivial solutions of the York equation (2), nor that (ii) the resulting slices will (still) contain black holes. However, from our numerical results in section XI, both (i) and (ii) do in fact hold in practice.

Moreover, although our motivation for this boundary condition took the perturbation to either be small, or at least to be small in its effects near the inner boundary, our numerical results in section XI D also show that this restriction isn’t needed, i.e. that accurate results (initial data slices which satisfy the constraints) are still obtained even for perturbations which are large and/or have large effects near the inner boundary. In fact, it appears that essentially *any* reasonable inner boundary condition still yields accurate results.

We have previously (Thornburg (1993), sections 5.3 and 9.8) suggested that the fact that the physics of the initial data problem doesn’t specify any particular inner boundary condition for the York equation, constitutes a serious drawback of the overall black-hole–exclusion technique, and that the Ansatz (12) therefore “lacks a clear physical motivation and is at best an ad-hoc solution”. However, we now regard this criticism as unwarranted: Physically, the inner boundary condition for the York equation specifies what type of black hole (or more generally, spacetime region, cf. our discussion of the pqw5c slices in section XI E) is contained within the inner boundary. This *must* be specified as an input to the initial data algorithm, and the Ansatz (12) seems quite reasonable for this purpose.

We have made a few limited experiments with inner boundary conditions other than the simple Dirichlet condition (12), but much further research is needed to understand the relative merits of different inner boundary conditions, and their effects on the resulting initial data slices.

⁹We haven’t yet investigated non-localized perturbations.

VIII. DIAGNOSTICS

The purpose of any initial data algorithm is to construct slices which satisfy the constraints, so we use the numerically computed values of the constraints (1), (i.e. their deviations C and C^i from satisfaction), as diagnostics of our initial slices' accuracy. Because of its dependence through R on the 2nd derivatives of the 3-metric components, the energy constraint C is particularly sensitive (useful) for this purpose; in practice, nonzero computed values of C primarily measure errors in the computation of R .

We use a number of diagnostics to study the physical content of our slices and the spacetimes in which they're embedded, including the coordinate position(s) of any apparent horizon(s) in the slice, the mass distribution in each slice (measured in spherical symmetry by the Misner-Sharp mass function m_{MS} or the integrated scalar field mass function m_μ defined below), the scalar field's 3-energy density ρ (or the radial scalar field density $4\pi g_{\theta\theta}\rho$ in spherical symmetry), K , R , the 3-Ricci quadratic curvature invariant $R_{ij}R^{ij}$, the 4-Ricci scalar ${}^{(4)}R$, and the 4-Riemann quadratic curvature invariant $R_{abcd}R^{abcd}$.

As discussed by Guven and Ó Murchadha (1995), in spherical symmetry the Misner-Sharp mass function m_{MS} can be written as the volume integral of a local function $\mu = \mu(\rho, j^i; g_{ij}, K_{ij})$ of the scalar field variables. We can thus define an alternative mass function (which should be equal to the Misner-Sharp one) by volume-integrating μ ,

$$m_\mu = m_{\text{MS}}(r_{\min}) + \int_{r_{\min}}^r 4\pi g_{\theta\theta} \mu \sqrt{g_{rr}} dr \quad (13)$$

where $m_{\text{MS}}(r_{\min})$ is the Misner-Sharp mass function at the inner grid boundary $r = r_{\min}$. m_{MS} and m_μ are computed independently and in very different ways ((B18) vs. (B20) and (B21)), so their numerical equality at all radii is a useful consistency check and accuracy diagnostic. As discussed in appendix B3, for our computational scheme m_μ is numerically better-behaved than m_{MS} , so we generally use m_μ as a general-purpose mass function, and hereinafter we take m (with no subscripts) to denote m_μ .

By contracting the spacetime Einstein equations, it's easy to see that ${}^{(4)}R = 8\pi(\rho - T)$, so ${}^{(4)}R$ plays the role of a 4-invariant diagnostic for the scalar field density.

$R_{abcd}R^{abcd}$ is a 4-invariant diagnostic for spacetime curvature. As discussed by York (1989), $R_{abcd}R^{abcd}$ is given in terms of the 3 + 1 variables by

$$\begin{aligned} R_{abcd}R^{abcd} &= 8R_{ij}R^{ij} - 16R_{ij}(K^i_k K^{kj} - K K^{ij}) + 8K_{ij}K^{jk}K_{kl}K^{li} \\ &\quad - 16K K_{ij}K^i_k K^{kj} + 8K^2 K_{ij}K^{ij} - 8\nabla_{[i}K_{j]k} \nabla^i K^{jk} \\ &\quad + 16\pi \left[4T_{ij}(K^i_k K^{kj} - K K^{ij}) - 4R_{ij}T^{ij} \right] \\ &\quad + (16\pi)^2 \left[T_{ij}T^{ij} - \frac{1}{4}T^2 - \frac{9}{4}\rho^2 + \frac{3}{2}T\rho \right] \end{aligned} \quad (14)$$

Most of our diagnostics vary rapidly with spatial position in any black hole spacetime, even Schwarzschild spacetime (cf. appendix A). For example, in an Eddington-Finkelstein slice of a Schwarzschild spacetime, R typically varies as $\sim 1/r^4$, where r is the areal radius. To focus on the deviations away from a Schwarzschild / Eddington-Finkelstein slice, we usually normalize out the “background” Schwarzschild variation by using “relative” diagnostics, e.g. R/R_{Schw} . Here for any diagnostic Z , at each areal radius, Z_{Schw} denotes the value of Z at that same areal radius in an Eddington-Finkelstein slice of a unit-mass Schwarzschild

spacetime, and more generally, for any fixed m_* , $Z_{\text{Schw}(m_*)}$ denotes the value of Z at that same areal radius in an Eddington-Finkelstein slice of a mass- m_* Schwarzschild spacetime.

When considering a (spherically symmetric) slice or region of a slice whose mass function varies significantly with position, we also use “mass-relative” diagnostics, e.g. $R/R_{\text{Schw}(m(r))}$. Here for any slice \mathcal{S} and diagnostic Z , at each areal radius r , $Z_{\text{Schw}(m(r))}$ denotes the value of Z at that same areal radius r in an Eddington-Finkelstein slice of a Schwarzschild spacetime of mass $m(r)$, where $m(r)$ is the mass function of the slice \mathcal{S} at the areal radius r . Marsa (1995); Marsa and Choptuik (1996) have used the same notion of mass-relative variables in their initial data construction, though not with diagnostics.

IX. SCALAR FIELD AND SPHERICAL SYMMETRY

We have previously (Thornburg (1993), appendix 5) described the use of the same York-decomposition initial data problem algorithm and Ansätze described here, in constructing dynamic vacuum axisymmetric initial data slices containing a black hole surrounded by gravitational radiation. Here we discuss the algorithm and Ansätze’s use in a different system, the construction of dynamic spherically symmetric initial data slices (each) containing a black hole surrounded by one or more scalar field shells.

The spherically symmetric scalar field and similar systems have been studied by a number of past researchers, including (among others) analytical studies by Christoudolou (1986a, 1986b, 1987a, 1987b, 1991, 1993), 3 + 1 studies by Choptuik (1986, 1991); Seidel and Suen (1992); Bernstein and Bartnik (1995); Scheel *et al.* (1995a, 1995b); Anninos *et al.* (1995); Marsa (1995); Marsa and Choptuik (1996), 2 + 2 studies by Goldwirth and Piran (1987); Goldwirth *et al.* (1989); Hamadé and Stewart (1996), a hybrid 3 + 1 and 2 + 2 study by Gómez *et al.* (1996), and an interesting comparison of 3 + 1 and 2 + 2 methods by Choptuik *et al.* (1992).

[However, these authors haven’t used the York decomposition for constructing their initial data: Focusing on the 3+1 studies, Choptuik (1986, 1991); Bernstein and Bartnik (1995); Scheel *et al.* (1995a, 1995b) all constructed initial data using slicing conditions which simplified the constraints sufficiently to allow a “direct” (algebraic) solution of the constraints by suitably ordering the 3+1 equations. Using similar Eddington-Finkelstein-like slices to ours, Marsa (1995); Marsa and Choptuik (1996) used an Ansatz of setting $K^r_r = (K^r_r)_{\text{Schw}(m(r))}$, then used a functional iteration scheme to satisfy the remaining constraint equations. Seidel and Suen (1992); Anninos *et al.* (1995) used Schwarzschild spacetime as their only general relativistic system, and hence needed only to use an appropriate slice of Schwarzschild spacetime for their initial data.]

Turning now to our scalar field formalism, we begin with the generic case, making no assumptions about any spacetime symmetries. Following Choptuik (1986, 1991); Marsa (1995); Marsa and Choptuik (1996), we take the scalar field ϕ to satisfy the 4-scalar wave equation $\nabla_a \nabla^a \phi = 0$, and to have the stress-energy tensor

$$4\pi T_{ab} = (\partial_a \phi)(\partial_b \phi) - \frac{1}{2} g_{ab} (\partial_c \phi)(\partial^c \phi) \quad (15)$$

We then define the 3 + 1 scalar field variables

$$P_i = \nabla_i \phi \quad (16a)$$

$$Q = (\partial_t \phi - \beta^i \nabla_i \phi) / \alpha \quad (16b)$$

so that

$$\partial_t \phi = \alpha Q + \beta^k P_k \quad (17a)$$

$$\partial_i \phi = P_i \quad (17b)$$

(These definitions (16) and (17) are similar, but not identical, to those of Choptuik (1986, 1991); Marsa (1995); Marsa and Choptuik (1996).) A straightforward calculation then gives the 3 + 1 energy and momentum densities as

$$4\pi\rho = \frac{1}{2}(P_k P^k + Q^2) \quad (18a)$$

$$4\pi j_i = -P_i Q \quad (18b)$$

and the spatial stress-energy tensor and its trace as

$$4\pi T_{ij} = P_i P_j + \frac{1}{2} g_{ij} (-P_k P^k + Q^2) \quad (19)$$

$$4\pi T = -\frac{1}{2} P_k P^k + \frac{3}{2} Q^2 \quad (20)$$

Corresponding to (4), the York-transformation scalings for P_i and Q are

$$(P_i)_{\text{out}} = \Psi^{-2} P_i \quad (21a)$$

$$(Q)_{\text{out}} = \Psi^{-4} Q \quad (21b)$$

We now assume that spacetime is spherically symmetric, with the spatial coordinates $x^i = (r, \theta, \phi)$ having the usual polar spherical topology. However, we leave r arbitrary, i.e. we make no assumption about the choice of (the radial component of) the shift vector. We take the 3 + 1 field tensors to have the coordinate components

$$g_{ij} \equiv \text{diag} \left[A \quad B \quad B \sin^2 \theta \right] \quad (22)$$

$$K_{ij} \equiv \text{diag} \left[X \quad Y \quad Y \sin^2 \theta \right] \quad (23)$$

$$\beta^i \equiv \left[\beta \quad 0 \quad 0 \right] \quad (24)$$

$$P_i \equiv \left[P \quad 0 \quad 0 \right] \quad (25)$$

and for the York decomposition we take

$$\Omega^i \equiv \left[\Omega \quad 0 \quad 0 \right] \quad (26)$$

Notice that we do *not* factor out either a conformal factor or any r^2 factors from the 3-metric components.¹⁰

¹⁰Although this somewhat simplifies the 3 + 1 equations, it may degrade the accuracy of our computational scheme at large r . In particular, in hindsight not factoring out r^2 factors may have been an unwise design choice. It might be interesting to try a side-by-side accuracy comparison between otherwise-identical factored and unfactored schemes, but we haven't investigated this.

With these assumptions, it’s then straightforward, though tedious, to express all the other $3 + 1$ variables in terms of the “state variables” A , B , X , Y , P , and Q , and their spatial (1st and 2nd) derivatives. For reference, in appendix B we tabulate the resulting equations for all the $3 + 1$ variables involved in our initial data algorithm.

X. NUMERICAL METHODS

We use standard finite differencing techniques to numerically solve the York updating equation (7). We describe our numerical methods in detail in a following paper (Thornburg (1998)); we merely summarize them here.

For the initial data equations, we use the usual centered 5 point 4th order finite difference molecules in the grid interior, and off-centered 5 (6) point 4th order molecules for 1st (2nd) derivatives near the grid boundaries. We use the same finite difference molecules in all contexts in the equations, including “left hand side”, “right hand side”, interior equations, and boundary conditions.

After finite differencing the elliptic PDE (7), we row scale the resulting linear system to improve its numerical conditioning, then LU decompose and solve it via LINPACK band matrix routines (Dongarra *et al.* (1979)). We use IEEE double (64 bit) precision for all floating point computations.

We use a smoothly nonuniform grid, chosen to be uniform in the “warped” radial coordinate

$$w(r) = \frac{r_0}{a} \left(1 - \frac{1}{r/r_0} \right) + \frac{r_0}{b} \log \left(\frac{r}{r_0} \right) + \frac{r_0}{c} \left(\frac{r}{r_0} - 1 \right) \quad (27)$$

where r_0 , a , b , and c are suitably chosen parameters. We don’t use any sort of staggered grid. Note that we use w only for finite differencing – all tensor components are still taken with respect to the (r, θ, ϕ) coordinate basis.

By convention, we always place the inner grid boundary at $w = 0$, i.e. $r = r_0 \equiv r_{\min}$. All our results in this paper use the parameters $r_0 = 1.5$, $a = \infty$ (effectively omitting the first term in (27)), $b = 5$, and $c = 100$. As shown in figure 1, for these parameters w qualitatively resembles a logarithmic radial coordinate in the inner part of the grid, and a uniform radial coordinate in the outer part of the grid.

XI. SAMPLE RESULTS

As shown in table I, we have computed a number of test initial data slices, using various combinations of numerical parameters (grid resolutions and outer boundary positions) and initial perturbations. Most of our discussion of these slices is independent of their numerical parameters, so we usually refer generically to the families of slices sharing common initial perturbations, and plot only the highest-resolution results within each family.

In describing our results, we use the subscript “_{init}” to refer to the initial slice (step 1 in our overall initial data algorithm of section VII), “_{perturb}” to refer to the perturbed slice (the result of step 2), “_{York}” to refer to the result of the York projection operator (step 3),

and “final” to refer to the final result after the numerical coordinate transformation back to an areal radial coordinate (step 4).

All our results presented here use an Eddington-Finkelstein slice of a unit-mass Schwarzschild spacetime for the initial slice (step 1), and include a final numerical 3-coordinate transformation to make the radial coordinate areal (step 4).

A. Scalar Field Phenomenology

As a first example of our initial data solver, consider the pqw5 slice, defined by the perturbation (step 2 in our overall initial data algorithm of section VII)

$$P \rightarrow P + 0.02 \times \text{Gaussian}(r_{\text{init}}=20, \sigma=5) \quad (28)$$

(Q remains identically zero.)

Figure 2 shows the York-decomposition variables Ψ and Ω for this slice. Notice that because the York equation (2) is elliptic, the localized perturbation (28) results in the York projection operator being nontrivial ($\Psi \neq 1$, $\Omega \neq 0$) throughout almost the entire slice. However, for the relatively small perturbation (28), the York projection and the numerical coordinate transformation back to an areal radial coordinate (the latter given here by $r_{\text{final}}/r_{\text{York}} = \Psi^2$) both differ from the identity by only a few percent.

Figure 3 shows the relative 3-metric and extrinsic curvature components for this slice, and figure 4 shows the resulting relative 3-invariants K , R , and $R_{ij}R^{ij}$. Due to the nonlocality of the York projection operator, all the geometric field variables deviate significantly from their initial (Schwarzschild / Eddington-Finkelstein) values throughout the slice. Notice also that there’s an apparent horizon just inside $r = 2$, i.e. the slice does (still) contain a black hole.

Figure 5 shows this slice’s scalar field and mass distributions. As can be seen, the slice contains a shell of scalar field surrounding the black hole. The scalar field shell has a roughly Gaussian profile, which for the radial density $4\pi B\rho$ is centered at $r \approx 21.8$, with thickness $\sigma \approx 3.5$. Despite the relatively small perturbation (28), the scalar field shell is fairly massive, approximately 0.66 times the black hole mass (approximately 40% of the slice’s total mass). [Although it’s not apparent here, time-evolving this initial data (Thornburg (1998)) shows that the shell is actually the superposition of two momentarily coincident shells, one ingoing and one outgoing. However, contrary to what one might expect, the two shells have quite different masses.]

B. Spacetime and Slicing Phenomenology

From figure 5 it’s clear that away from the scalar field shell the pqw5 slice is nearly vacuum (all our scalar field diagnostics are very small), so by Birkhoff’s theorem it must be nearly Schwarzschild there. More precisely, inside the scalar field shell the pqw5 slice must be nearly (isometric to) some slice of a Schwarzschild spacetime with mass $m_{<} \equiv m_{\text{bh}} \approx 0.976$, while outside the scalar field shell it must be nearly (isometric to) some slice of a Schwarzschild spacetime with mass $m_{>} \equiv m_{\text{total}} \approx 1.617$.

In support of this, figure 6 shows the mass-relative 4-Riemann curvature invariant $R_{abcd}R^{abcd}$ for the pqw5 slice. As expected, away from the scalar field shell $R_{abcd}R^{abcd}$ is almost exactly equal to its value for a Schwarzschild spacetime of matching mass ($m_<$ inside the shell, $m_>$ outside).

Figure 7 shows the mass-relative 3-invariants K , R , and $R_{ij}R^{ij}$ for the pqw5 slice. The mass-relative ratios all deviate substantially from unity even in the near-vacuum regions. From this we conclude that although the pqw5 slice is nearly (isometric to) *some* slice of a matching-mass Schwarzschild spacetime in each of its near-vacuum regions, neither of these slices is our canonical Eddington-Finkelstein one.

It might be interesting to explicitly compute the embedding of these regions of the slice in their respective Schwarzschild spacetimes, i.e. explicitly compute (say) each region’s Eddington-Finkelstein or Schwarzschild time coordinate as a function of spatial position (e.g. areal radius r). The two time coordinates would each only be defined up to an arbitrary additive constant, and (being referred to different Schwarzschild spacetimes) they wouldn’t be directly comparable, but their intra-region variation might still be interesting. However, we haven’t as yet made such a study.

From figures 4 and 7, it appears that at large r , $K/K_{\text{Schw}} \rightarrow 1$ and $R/R_{\text{Schw}} \rightarrow 1$, while $J \equiv R_{ij}R^{ij}$ displays the different behavior $J/J_{\text{Schw}(m(r))} \rightarrow 1$ and hence (cf. (A11)) $J/J_{\text{Schw}} \rightarrow (m_{\text{total}}/m_{\text{init}})^2$. Examining other slices computed with a larger outer boundary radius, e.g. the 100o30.pqw5 and 200o30.pqw5 slices (cf. figure 10) confirms these asymptotic behaviors. A simple analytical argument also confirms this behavior for K : The transformation (4) in the York projection operator preserves K at any given event, and since $\Psi \rightarrow 1$ at large r , the transformation back to an areal radial coordinate preserves K ’s leading order behavior there. Thus our initial data slices must have asymptotically the same K as the initial Schwarzschild / Eddington-Finkelstein slice, i.e. $K/K_{\text{Schw}(m_{\text{init}})} \rightarrow 1$ at large r .

Since our different 3-invariant diagnostics have different asymptotic behaviors relative to our canonical Eddington-Finkelstein slice, it’s clear that our slice isn’t (even) asymptotically Eddington-Finkelstein. This asymptotic “warping” of the slice may prove a complication for 3 + 1 time evolution calculations. It might be worth investigating whether modifications to our initial data algorithm (e.g. a different type of perturbation, and/or different outer boundary conditions) might yield slices with nicer asymptotic properties, but we haven’t as yet done this.

C. Accuracy

The main error sources in a 3 + 1 code such as ours are due to the finite grid resolution (finite differencing truncation errors), the finite outer boundary radius, and floating point roundoff. As discussed in appendix E, we expect the first two of these to vary in predictable ways with the corresponding numerical parameters (grid resolutions and outer boundary positions), and we can quantitatively measure these errors by comparing computations of the same physical system using different numerical parameters. In the context of a finite differencing code such as ours, i.e. one solving elliptic PDEs such as the York equation (2), floating point roundoff errors are easily distinguished from other error sources by their non-smoothness (large and quasi-random variations from one grid point to the next).

As an example of our computational scheme’s overall accuracy level, figure 8 shows the magnitude of the numerically computed energy and momentum constraints at various points in the initial data computation for the 100.pqw5 and 200.pqw5 slices. Consider first part (a) of the figure, which shows the magnitude $|C|$ of the energy constraint, and for the moment focus only on the 100.pqw5 curves: $|C_{\text{Schw}}|$ shows the basic “background” accuracy level of our finite differencing, tailing off into floating point roundoff noise for $r \gtrsim 40$. In contrast, $|C_{\text{perturb}}|$ shows the effects of the perturbation (28): $|C_{\text{perturb}}|$ is large ($\gg |C_{\text{Schw}}|$) wherever the perturbation is significant. Finally, $|C_{\text{final}}|$ shows the effects of the York projection operator (and the numerical coordinate transformation back to an areal radial coordinate), with $|C_{\text{final}}| \ll |C_{\text{perturb}}|$ wherever the perturbation is significant, and more generally $|C_{\text{final}}|$ small (comparable in magnitude to $|C_{\text{Schw}}|$) everywhere in the slice. In other words, we see that the York projection operator does indeed act to restore the field variables back into the constraint hypersurface.

To assess our computational scheme’s finite differencing errors, figure 8(a) also shows $|C_{\text{Schw}}|$, $|C_{\text{perturb}}|$, and $|C_{\text{final}}|$ for the 200.pqw5 slice, which (cf. table I) is computed using twice the grid resolution (half the grid spacing) as the 100.pqw5 slice, but is otherwise identical. Notice that for $|C_{\text{Schw}}|$ and $|C_{\text{final}}|$, the 100.pqw5 and 200.pqw5 curves are both very similar in shape, the 200.pqw5 curve being offset downwards (smaller $|C|$) by a factor of 16 (compare with the scale bar), until both tail off into roundoff noise at large r . As discussed in appendix E, this constitutes strong evidence that these $|C|$ values are indeed dominated by 4th order finite differencing truncation errors at small and moderate r , and floating point roundoff errors at large r .¹¹ Notice also that the overall level of the $|C|$ values, i.e. of the deviation of the energy constraint from satisfaction, is very low, with $|C_{\text{final}}| \lesssim 10^{-8}$ (10^{-9}) for the 100.pqw5 (200.pqw5) slice.

Figure 8(b) shows the magnitude of the numerically computed momentum constraint C^r ¹² at the same points in the initial data computation for these slices. (Since the perturbation (28) doesn’t change C^r , $|C_{\text{perturb}}^r| = |C_{\text{Schw}}^r|$, so these are plotted as the same curve.) From the figure it’s clear that the overall level of the momentum constraints is ~ 3 orders of magnitude smaller than that of the energy constraint. Also, $|C_{\text{final}}^r|$ is small (comparable in magnitude to $|C_{\text{Schw}}^r|$) everywhere in the slice, and both show 4th order convergence in the same manner as $|C_{\text{Schw}}|$ and $|C_{\text{final}}|$.

As an example of a more quantitative test of the finite differencing errors, figure 9 shows a scatterplot of the 200.pqw5 versus the 100.pqw5 C_{final} values. As discussed in appendix E, for 4th order convergence all the points (except for outliers from the grid boundaries) should fall on a line through the origin with slope $\frac{1}{16}$. As can be seen, except for the grid-boundary outliers, all the points do indeed fall very closely on this line. We emphasize here that (cf. appendix E) the plotted line is *not* a fit to the data, but rather an a priori prediction

¹¹ Due to boundary finite differencing effects (cf. appendix E), C and C^r are both roughly a factor of 10 larger at the grid boundaries than at nearby non-boundary grid points. However, even the boundary C and C^r values still show 4th order convergence.

¹²In spherical symmetry C^r is the only nonzero component of the momentum constraint vector C^i , cf. (B16).

with *no* adjustable parameters, making this a very stringent test.

Errors due to the finite outer boundary radius r_{\max} are more problematical: these enter through the outer boundary conditions (10a) and (11), which essentially fix the asymptotic flatness of the initial data slice. Without a clear-cut measurement of the slice’s embedding in the far-field Schwarzschild region (cf. section XI B), asymptotic-flatness errors are difficult to measure. Moreover, it’s not immediately obvious just how (i.e. with what power of r_{\max}) these errors should scale with r_{\max} .

However, to give an indication of the typical magnitudes of these errors, the relative changes $\delta K/K$, $\delta R/R$, $\delta J/J$, and $\delta I/I$ (where $J \equiv R_{ij}R^{ij}$ and $I \equiv R_{abcd}R^{abcd}$) between the same positions in (common to) the pqw5 slices with $w_{\max} = 4$ ($r_{\max} \approx 248$) and $w_{\max} = 10$ ($r_{\max} \approx 813$), are all on the order of 10^{-5} , while the relative changes $\delta m/m$ in the computed black hole and total spacetime masses are $\sim 3 \times 10^{-6}$. The corresponding changes between the slices with $w_{\max} = 10$ ($r_{\max} \approx 813$) and $w_{\max} = 30$ ($r_{\max} \approx 2780$), are all about a factor of 10 smaller, and in general the outer boundary errors appear to scale approximately as $\sim 1/r_{\max}^2$. These are all *continuum* effects: with one exception discussed below, the differences between different-resolution slices with the same r_{\max} , are all much smaller than the differences between slices with different r_{\max} .

The one significant non-continuum effect apparent in these slices is the presence of significant floating-point roundoff noise in our curvature diagnostics, particularly in R , at large r . As an example of this, figure 10 shows the relative and mass-relative values of various embedding and curvature diagnostics for the outer parts of the 100o30.pqw5 and 200o30.pqw5 slices. While the K , $R_{ij}R^{ij}$, and $R_{abcd}R^{abcd}$ values show no visible noise, the R values show serious noise, with the relative noise amplitude $\delta R/R_{\text{Schw}}$ roughly 4 times larger in the 200o30.pqw5 slice, and in both slices growing rapidly with r to $\sim 5\%$ (20%) at the outer boundary ($r_{\max} \approx 2780$) of the 100o30.pqw5 (200o30.pqw5) slice. The rapid growth of the relative noise amplitude with r is actually entirely due to the rapid ($\sim 1/r^4$) falloff in R_{Schw} : within each slice the actual absolute noise level in R is essentially constant for the range of r in the figure.

Comparing the computations (appendix B) of the different diagnostics plotted in figure 10, we see that K is computed from the 3-metric and extrinsic curvature components by algebraic operations only, while R , $R_{ij}R^{ij}$, and $R_{abcd}R^{abcd}$ all depend on (2nd) numerical derivatives of the 3-metric components. Numerical differentiation is well known as a noise-amplifying process, and will inherently amplify normal low-level roundoff noise in the 3-metric components. To test whether this process can account for the observed noise in R , figure 10 also shows the relative value of $R_{\text{fit}} \pm \varepsilon/(\Delta w)^2$, where R_{fit} is an empirical least-squares fit to the R values, and the $\pm \varepsilon/(\Delta w)^2$ term models the effects on R of $O(\varepsilon)$ roundoff errors in the 3-metric components being 2nd-differentiated, with $\varepsilon = 6 \times 10^{-19}$ an “eyeball-fitted” constant parameter, and Δw the grid spacing in our w nonuniform gridding coordinate (cf. section X). From the figure it’s clear that this model does in fact nicely account for the r - and Δw -dependence of R ’s roundoff noise.

Although this explains the noise in R , it raises the further question of why $R_{ij}R^{ij}$ and $R_{abcd}R^{abcd}$ don’t show similar effects. (A careful analysis does show some roundoff noise in $R_{ij}R^{ij}$ and $R_{abcd}R^{abcd}$, but only at levels many orders of magnitude below that in R .) We’re not certain, but we suspect the explanation lies in the detailed form of the respective equations, with the offending 2nd derivative terms being (presumably) relatively less important

in the computations of $R_{ij}R^{ij}$ and $R_{abcd}R^{abcd}$ than in R . In any case, though, the absolute magnitude of even R 's roundoff noise is still very small, $\pm\epsilon/(\Delta w)^2 \approx 6 \times 10^{-15}$ (2×10^{-14}) for the 100o30.pqw5 (200o30.pqw5) slice. Although R appears as a coefficient in the York equation (2), the offending term is linear (so R 's noise should mainly average out), and the noise doesn't appear to be a serious error source in the solutions Ψ and Ω^i , or in the computed 3-metric and extrinsic curvature components.

D. Inner Boundary Condition

Thus far we have considered only the perturbation (28), which is relatively small at the inner boundary ($\delta P_{\text{inner}}/\delta P_{\text{max}} \approx 10^{-3}$). As discussed in section VII, our motivation for the inner boundary condition (12) is actually predicated on the perturbation having negligible effects there.

It's thus of interest to determine whether and how well our initial data algorithm works for perturbations which don't satisfy this restriction, i.e. for perturbations which have non-negligible effects at the inner boundary. As an example of such a perturbation, consider the pqw5i slice. As shown in table I, this uses the perturbation

$$P \rightarrow P + 0.02 \times \text{Gaussian}(r_{\text{init}}=10, \sigma=5) \quad (29)$$

instead of (28). The perturbation (29) has the same amplitude and width as (28), but is centered at $r_{\text{init}} = 10$ instead of $r_{\text{init}} = 20$, so it's fairly large at the inner boundary ($\delta P_{\text{inner}}/\delta P_{\text{max}} \approx 0.24$).

Figure 11 shows $|C_{\text{Schw}}|$, $|C_{\text{perturb}}|$, and $|C_{\text{final}}|$ for the pqw5i slice, analogously to figure 8(a) for the pqw5 slice. It's clear that despite the pqw5i slice's substantial perturbation at the inner boundary, its initial data computation remains fully accurate, with $|C_{\text{final}}| \ll |C_{\text{perturb}}|$ wherever the perturbation is significant, and $|C_{\text{final}}|$ small (comparable in magnitude to $|C_{\text{Schw}}|$) everywhere in the slice, including near to and at the inner boundary.

Moreover, comparing the $|C_{\text{Schw}}|$ and $|C_{\text{final}}|$ curves in figure 11, we see that the 100.pqw5i and 200.pqw5i curves are again both very similar in shape, the 200.pqw5i curve being offset downwards (smaller $|C|$) by a factor of 16, until both tail off into roundoff noise at large r . Just as for the pqw5 slice (cf. our discussion of figure 8 in section XI C), this implies that these errors (the nonzero values of C) are dominated by (the expected) 4th order finite differencing truncation errors at small and moderate r , and floating point roundoff errors at large r .¹³ The same is also true of C^r for these slices (details of the analysis omitted for brevity).

These pqw5i results demonstrate that despite our inner boundary condition (12) being motivated by – and only for – the special case where the perturbation's effects are negligible at the inner boundary, we actually obtain fully accurate initial data even for perturbations which are large there.

¹³The pqw5i $|C|$ values in figure 11 also show similar boundary finite differencing anomalies (cf. appendix E), to the pqw5 $|C|$ values in figure 8 (cf. footnote 11).

E. Other Perturbations

As shown in table I, we have also experimented with several alternative variants of the perturbation (28) for step 2 in our algorithm summary of section VII.

Figure 12 shows the effect of increasing the perturbation amplitude from 0.02 (the pqw5 slice discussed above) to 0.05 (the pqw5b slice) or 0.1 (the pqw5c slice). With one exception discussed below, all three slices are qualitatively fairly similar. In going from the pqw5 slice to the pqw5b and pqw5c slices, the main detailed differences are that as a result of the larger perturbations, the scalar field shells become much more massive (from approximately 0.66 to 3.9 and 17 times the black hole mass, or equivalently from approximately 40% to 80% and 94% of the total spacetime mass, respectively), and are also somewhat larger and thicker. As well, the deviations (not shown here) of all the geometric field variables from their Schwarzschild / Eddington-Finkelstein values become much larger. Despite these stronger nonlinear effects, we experienced no difficulties with poor convergence of the Newton-Kantorovich iteration for these models.¹⁴

The pqw5c slice shows a new effect: although the mass function still shows a significant mass contained within the numerical grid’s inner boundary (at $r = 1.5$), here there’s no longer any apparent horizon within the numerical grid. The pqw5c slice’s “black hole” mass shown in table I thus no longer represents the mass of an actual black hole, but rather merely of the region within the inner boundary. Since $r \approx 2.6m > 2m$ on the inner boundary this region may, but need not necessarily, contain a black hole. (Even with the constraints imposed, the continuation of the field variables into the origin is obviously non-unique.)

Since the inner grid boundary for this slice doesn’t lie within an apparent horizon, this numerical data is unsuitable for a black-hole-excluded time evolution. However, viewed purely as initial data, it remains fully accurate, i.e. the constraints are small everywhere in the numerical grid.

Figure 13 shows the effects of using a narrow (width-1) but high-amplitude (0.1) perturbation (the pqw1 slice). This slice qualitatively resembles the pqw5b slice: it contain a black hole surrounded by a moderately massive scalar field shell (approximately 3.0 times the black hole mass, or equivalently approximately 75% of the total spacetime mass). However, corresponding to the narrow perturbation, here the scalar field shell is very thin, with a fractional width (σ/r_{center} for a Gaussian fit to the radial scalar field density $4\pi B\rho$) of only 0.033.

The pw5+qw3 slice shows the effect of applying perturbations to both P and Q , instead of P alone as in the previous slices. This slice is qualitatively fairly similar to the pqw5b slice, except that since both P and Q are nonzero, j^r is nonzero as well as ρ .

Having j^r nonzero makes this slice particularly useful for testing the equality of the Misner-Sharp and integrated-scalar-field mass functions m_{MS} and m_μ (cf. section VIII), since now both terms in the definition (B20) of μ contribute, instead of just the ρ term as in all the previous slices. Figure 14 shows the relative deviation of m_{MS} from m_μ for

¹⁴In retrospect this isn’t too surprising, as even for the pqw5c slice the peak values of $\Psi - 1$ and Ω are still only ≈ 0.22 and 0.16 respectively, so the nonlinearities are still fairly weak in an absolute sense.

this slice, for both grid resolutions. Both deviations are very small across their slices, with $m_{\text{MS}} = m_\mu$ to a relative accuracy of $\lesssim 10^{-5}$ (10^{-6}) for the 100.pq5+qw3 (200.pq5+qw3) slice. Moreover, a quantitative convergence test (cf. appendix E and section XI C; details omitted for brevity) shows that these deviations are once again dominated by (the expected) 4th order finite differencing truncation errors.

Instead of perturbing the matter variables, we can perturb the initial slice’s geometry (3-metric and/or extrinsic curvature components).¹⁵ Since our initial data Ansätze always take the initial analytical black hole slice to be vacuum, and the York projection operator (4) and (21) obviously preserves this, the resulting slice will therefore also always be vacuum. We have previously shown (Thornburg (1993), appendix 5) that in the non-spherically-symmetric case, suitable geometry perturbations yield (vacuum) dynamic initial slices containing black holes surrounded by gravitational radiation.

However, in spherical symmetry any vacuum slice is necessarily some slice in (a) Schwarzschild spacetime. Although a “warped Schwarzschild” slice of this type has no true dynamics, it can still be useful as a numerical-relativity test-bed problem: None of the test problems suggested by Centrella *et al.* (1986) are applicable to the spherically symmetric scalar field system, but York (1989) has suggested testing the numerical evolution of “hand-warped” slices in Minkowski spacetime. In the spirit of this latter suggestion, our “warped Schwarzschild” slices are of interest as alternative test cases. (As will be seen, they also offer a particularly good environment for testing an initial data problem algorithm and computer code.)

To assess the accuracy of these slices, we use m_{MS} and $R_{abcd}R^{abcd}$ as diagnostics: m_{MS} should be constant across each slice, and $R_{abcd}R^{abcd}$ should be everywhere the same as in a matching-mass Schwarzschild spacetime (i.e. the mass-relative $I \equiv R_{abcd}R^{abcd}$ should be unity across the slice).

For example, consider the daw5c slice, which uses a perturbation applied to $A \equiv g_{rr}$,

$$A \rightarrow A + 0.1 \times \text{Gaussian}(r_{\text{init}}=20, \sigma=5) \quad (30)$$

This amplitude gives roughly the same warping of the slice (e.g. deviation of K/K_{Schw} from unity) as for the pqw5 slice.

Figure 15 shows the relative deviations from unity (errors) of $m_{\text{MS}}/m_{\text{total}}$ and $I/I_{\text{Schw}(m_{\text{total}})}$ (i.e. the relative errors in m_{MS} and I) across the daw5c slice, computed with two different grid resolutions, where m_{total} is the total mass of the slice (since the slice is vacuum, this is equal to the Misner-Sharp mass within the inner grid boundary). Both diagnostics show only very small deviations across the slices, with $m = m_{\text{total}}$ to a relative accuracy of $\lesssim 10^{-5}$ (5×10^{-7}) for the 100.daw5 (200.daw5) slice, and $I = I_{\text{Schw}(m_{\text{total}})}$ to a relative accuracy of $\lesssim 3 \times 10^{-4}$ (5×10^{-5}) respectively. Moreover, a quantitative convergence test (cf. appendix E and section XI C; details again omitted for brevity) shows that these errors are once again dominated by (the expected) 4th order finite differencing truncation errors.

Finally, note that the computation of $I \equiv R_{abcd}R^{abcd}$ via (14) and (B23)–(B29) depends nontrivially on all the state variables (3-metric, extrinsic curvature, and scalar field compo-

¹⁵Or we could perturb both matter and geometry.

nents) in our computational scheme. The observation that $I = I_{\text{Schw}(m_{\text{total}})}$ to high accuracy for the vacuum slices, and more generally that $I = I_{\text{Schw}(m(r))}$ for the vacuum regions of all our slices, thus gives a strong test of the overall correctness of a large part (essentially the geometry terms in all the equations) of our code, including freedom from most errors in either deriving our continuum equations, or programming the numerical computations.

XII. CONCLUSIONS AND DIRECTIONS FOR FURTHER RESEARCH

Like many other researchers, we find York’s conformal-decomposition technique to offer an elegant, reliable, and fairly efficient means of constructing $3 + 1$ initial data. In this paper we consider the general case of the York decomposition, where (as is required by most black-hole–exclusion slicings) K is nonzero and spatially variable throughout most or all of the slices, and hence the full nonlinear 4-vector York equations must be solved numerically.

The main focus of this paper is on the combination of this numerical solution, with a set of Ansätze to provide the York decomposition’s inputs and inner boundary conditions: We begin with a known black hole initial data slice (Ansatz), apply an arbitrary (generally constraint-violating) perturbation (Ansatz) to it, then use the York decomposition to project the perturbed field variables back into the constraint hypersurface, using a further Ansatz to supply inner boundary conditions for the York equations. (Our algorithm also incorporates a final numerical coordinate transformation to (e.g.) restore an areal radial coordinate, but this is only for convenience.)

In comparison to other initial data algorithms, the key advantage of this algorithm is its flexibility: It’s easily applicable to almost any slicing, and so permits the slicing to be chosen for convenience in (say) a black-hole–excluded time evolution, rather than being restricted by the initial data solver. This algorithm is also equally applicable in spherical symmetry, axisymmetry, or in fully 3-dimensional spacetimes, and in both vacuum and non-vacuum spacetimes.

Collectively, this algorithm’s Ansätze provide a great deal of flexibility in controlling the physical content of the resulting initial data. An interesting area for further research would be in trying to better understand the relationship between this physical content, and the choices made for the algorithm’s various Ansätze. That is, at present we can’t a priori (i.e. before solving the York equations) predict very much about the physical content of the resulting initial data obtained from a given set of Ansätze choices, so if some particular type of initial data is desired, some trial and error may be needed to obtain the desired results. A better understanding of this would both be of practical benefit in more easily constructing initial data with desired properties, and quite likely prove informative in mapping the range and phenomenology of possible initial data obtainable using our methods.

Turning now to the individual Ansätze, the choice of the initial known black hole slice seems fairly straightforward: Given the black-hole–exclusion requirement that the slicing and all the $3 + 1$ field variables be nonsingular near to and on the horizon, the natural choice is an Eddington-Finkelstein slice of Schwarzschild spacetime in spherical symmetry, or a

Kerr slice of Kerr spacetime in more general cases.¹⁶

In contrast, the choices for our other Ansätze (the perturbation to apply to the initial slice, and the inner boundary conditions for the York decomposition) are less clear-cut. The choices presented here (respectively adding a Gaussian to one or a few of the 3-metric, extrinsic curvature, or matter field variable components; and Dirichlet inner boundary conditions) are essentially the first ones we tried, and as yet we have made only limited experiments with other choices. The choices presented here seem to work adequately, in the sense of yielding dynamic black hole spacetimes suitable for numerical evolutions (Thornburg (1993, 1998)), but clearly these choices are only a tiny subset of the possible parameter space. Both numerical and theoretical studies of a broader range of choices would be useful here.

As well as a general discussion of the initial data problem algorithm on generic slices, in this paper we present numerical results for a specific model problem system, the spherically symmetric scalar field. We find that the resulting full nonlinear 4-vector York equations can be solved robustly and with high accuracy using a Newton-Kantorovich “outer linearization”, followed by a standard direct solution of the resulting sequence of “inner” linear elliptic PDEs, using 4th order finite differencing on a smoothly nonuniform grid. It seems likely that a wide range of other numerical methods would also work well on this problem.

We haven’t encountered any difficulties with the York equations failing to have valid and physically reasonable solutions, even with strong perturbations yielding very massive scalar field shells (up to ~ 17 times the black hole’s mass in our tests). However, we also don’t have any rigorous proofs that such difficulties couldn’t arise for different choices of the various Ansätze. Further research in this direction would be valuable.

As examples of our initial data solver, we discuss a number of Eddington-Finkelstein-like initial data slices containing black holes surrounded by scalar field shells, and also several vacuum black hole slices with nontrivial slicings. As described in table I, all of our test slices use (local) Gaussian perturbations added to one or two of the scalar field, 3-metric, or extrinsic curvature components. The slices vary in their perturbations’ positions, amplitudes, and widths, in which field variable or variables is/are perturbed, and in the numerical parameters (grid resolution and outer boundary position).

We use a number of diagnostics to analyze these slices, including apparent horizon positions, the Misner-Sharp and integrated-scalar-field mass functions m_{MS} and m_{μ} (respectively), the scalar field’s 3-energy density ρ and radial 3-energy density $4\pi g_{\theta\theta}\rho$, the extrinsic curvature scalar K , the 3-Ricci scalar R and quadratic curvature invariant $R_{ij}R^{ij}$, the 4-Ricci scalar ${}^{(4)}R$, and the 4-Riemann quadratic curvature invariant $R_{abcd}R^{abcd}$.

The focus of our analysis of the test slices is on exploring the general phenomenology of the initial data slices, and on testing and validating the accuracy of the initial data algorithm itself. The computed slices’ scalar field shells have masses ranging from as low as 0.17 to as high as 17 times the black hole mass m_{bh} , i.e. the scalar field shells comprise from as little as 14% to as much as 94% of the total slice masses. The scalar field shells have approximately

¹⁶Another option, which we haven’t explored, would be to use an initial slice constructed by some numerical method, either this one or another. Or one could use a non-black-hole initial slice (e.g. a slice in Minkowski spacetime), and try to choose the remaining Ansätze so as to produce a “geon” (cf. Abrahams and Evans (1992)).

Gaussian profiles with fractional widths σ/r_{center} (for the radial scalar field density $4\pi g_{\theta\theta}\rho$) ranging from 3.3% to 14%, and positions (radii) ranging from $13m_{\text{bh}}$ to $28m_{\text{bh}}$.

In all cases we find that the computed slices are very accurate: For grids with resolutions of $\Delta r/r \approx 0.02$ (0.01) near the perturbations, the numerically computed energy constraints are $\lesssim 10^{-8}$ (10^{-9}) in magnitude; the numerically computed momentum constraints are typically ~ 3 orders of magnitude smaller. The Misner-Sharp and integrated-scalar-field mass functions agree to within relative accuracies of $\lesssim 10^{-6}$ (10^{-7}) respectively. In tests of numerically constructed vacuum slices with nontrivial slicings, where we would expect the Misner-Sharp mass function to be constant and the 4-Riemann quadratic curvature invariant $R_{abcd}R^{abcd}$ to be equal to its Schwarzschild-spacetime value, we find these properties to hold to within relative errors of $\lesssim 10^{-5}$ (5×10^{-7}) and $\lesssim 3 \times 10^{-4}$ (5×10^{-5}) respectively. Except for floating point roundoff noise (most prominently in the 3-Ricci scalar R), the errors we do see in these and other diagnostics are all generally dominated by the expected $O((\Delta r)^4)$ finite differencing truncation errors.

As well as our main focus on the initial data problem, in the appendices of this paper we also present results in several related peripheral areas, including a tabulation of some of the key $3 + 1$ field variables for an Eddington-Finkelstein slice of Schwarzschild spacetime, the formulation of the Misner-Sharp mass function without restrictions on the slicing or spatial coordinates, numerical 3-coordinate transformations, and tests of the convergence of finite differencing computations to the continuum limit. We also review some little-known, but surprising, numerical analysis results on the non-smoothness of the errors incurred when interpolating data from one grid to another by the usual moving-local-interpolation schemes, and discuss these results' import for numerical coordinate transformations and horizon finding.

ACKNOWLEDGMENTS

We thank Niall Ó Murchadha for invaluable assistance with the definition of μ , and for suggesting the argument given in appendix B for why apparent horizons in spherical symmetry always have $r_{\text{areal}} = 2m$. We thank M. Huq for useful discussions on the non-smoothness of interpolation errors. We thank W. G. Unruh, R. Parachoniak, the University of British Columbia Physics Department, R. A. Matzner, and the University of Texas at Austin Center for Relativity for their hospitality and the use of their research facilities at various times during the course of this work. We thank J. Wolfgang, R. Parachoniak, P. Luckham, and J. Thorn for major assistance with setting up and maintaining computer facilities, and G. Rodgers and J. Thorn for financial support.

APPENDIX A: SCHWARZSCHILD SPACETIME IN EDDINGTON-FINKELSTEIN COORDINATES

Although the Eddington-Finkelstein coordinates (t, r, θ, ϕ) for Schwarzschild spacetime are well known (Misner *et al.* (1973), box 31.2), so far as we know the $3 + 1$ field variables for an Eddington-Finkelstein slice of Schwarzschild spacetime haven't been published before in the open literature. For reference we list the key ones here; we have given a more complete

listing elsewhere (Thornburg (1993), appendix 2). For a Schwarzschild spacetime of mass m ,

$$\alpha = \frac{1}{\sqrt{1 + \frac{2m}{r}}} \quad (\text{A1})$$

$$\beta^r = \frac{2m}{r} \frac{1}{1 + \frac{2m}{r}} \quad (\text{A2})$$

$$g_{rr} = 1 + \frac{2m}{r} \quad (\text{A3})$$

$$g_{\theta\theta} = r^2 \quad (\text{A4})$$

$$K_{rr} = -\frac{2m}{r^2} \frac{1 + \frac{m}{r}}{\sqrt{1 + \frac{2m}{r}}} \quad (\text{A5})$$

$$K_{\theta\theta} = 2m \frac{1}{\sqrt{1 + \frac{2m}{r}}} \quad (\text{A6})$$

so that

$$K = \frac{2m}{r^2} \frac{1 + \frac{3m}{r}}{\left(1 + \frac{2m}{r}\right)^{3/2}} \quad (\text{A7})$$

$$R_{rr} = -\frac{2m}{r^3} \frac{1}{1 + \frac{2m}{r}} \quad (\text{A8})$$

$$R_{\theta\theta} = \frac{m}{r} \frac{1 + \frac{4m}{r}}{\left(1 + \frac{2m}{r}\right)^2} \quad (\text{A9})$$

$$R = \frac{8m^2}{r^4} \frac{1}{\left(1 + \frac{2m}{r}\right)^2} \quad (\text{A10})$$

$$R_{ij}R^{ij} = \frac{6m^2}{r^6} \frac{1 + \frac{8}{3}\frac{m}{r} + \frac{16}{3}\frac{m^2}{r^2}}{\left(1 + \frac{2m}{r}\right)^4} \quad (\text{A11})$$

Independent of the slicing, Schwarzschild spacetime has $\rho = {}^{(4)}R = 0$ (vacuum) and $R_{abcd}R^{abcd} = 48m^2/r^6$ (Misner *et al.* (1973), section 31.7).

APPENDIX B: EQUATIONS FOR THE SPHERICALLY SYMMETRIC SCALAR FIELD SYSTEM

In this appendix we tabulate the equations for all the $3 + 1$ variables involved in our initial data algorithm, in terms of the state variables A , B , X , Y , P , and Q .

1. Geometric Variables

The only nonzero (3-)Christoffel symbols are

$$\Gamma_{rr}^r = \frac{1}{2} \frac{\partial_r A}{A} \quad (\text{B1a})$$

$$\Gamma_{\theta\theta}^r = -\frac{1}{2} \frac{\partial_r B}{A} \quad (\text{B1b})$$

$$\Gamma_{\phi\phi}^r = -\frac{1}{2} \frac{\partial_r B}{A} \sin^2 \theta \quad (\text{B1c})$$

$$\Gamma_{r\theta}^\theta = \Gamma_{\theta r}^\theta = \frac{1}{2} \frac{\partial_r B}{B} \quad (\text{B1d})$$

$$\Gamma_{\phi\phi}^\theta = -\sin \theta \cos \theta \quad (\text{B1e})$$

$$\Gamma_{r\phi}^\phi = \Gamma_{\phi r}^\phi = \frac{1}{2} \frac{\partial_r B}{B} \quad (\text{B1f})$$

$$\Gamma_{\theta\phi}^\phi = \Gamma_{\phi\theta}^\phi = \frac{\cos \theta}{\sin \theta} \quad (\text{B1g})$$

The 3-Ricci tensor, scalar, and quadratic curvature invariant are

$$R_{ij} = \text{diag} \left[R_{rr} \quad R_{\theta\theta} \quad R_{\theta\theta} \sin^2 \theta \right] \quad (\text{B2})$$

$$R_{rr} = -\frac{\partial_{rr} B}{B} + \frac{1}{2} \frac{(\partial_r B)^2}{B^2} + \frac{1}{2} \frac{(\partial_r A)(\partial_r B)}{AB} \quad (\text{B3})$$

$$R_{\theta\theta} = -\frac{1}{2} \frac{\partial_{rr} B}{A} + 1 + \frac{1}{4} \frac{(\partial_r A)(\partial_r B)}{A^2} \quad (\text{B4})$$

$$R = -2 \frac{\partial_{rr} B}{AB} + \frac{1}{2} \frac{(\partial_r B)^2}{AB^2} + \frac{(\partial_r A)(\partial_r B)}{A^2 B} + \frac{2}{B} \quad (\text{B5})$$

$$\begin{aligned} R_{ij} R^{ij} &= \frac{3}{2} \frac{(\partial_{rr} B)^2}{A^2 B^2} - 2 \frac{\partial_{rr} B}{AB^2} - \frac{3}{2} \frac{(\partial_r A)(\partial_r B)(\partial_{rr} B)}{A^3 B^2} - \frac{(\partial_r B)^2 (\partial_{rr} B)}{A^2 B^3} \\ &+ \frac{2}{B^2} + \frac{(\partial_r A)(\partial_r B)}{A^2 B^2} + \frac{3}{8} \frac{(\partial_r A)^2 (\partial_r B)^2}{A^4 B^2} + \frac{1}{2} \frac{(\partial_r A)(\partial_r B)^3}{A^3 B^3} + \frac{1}{4} \frac{(\partial_r B)^4}{A^2 B^4} \end{aligned} \quad (\text{B6})$$

In spherical symmetry it's relatively easy to locate apparent horizons, by simply zero-finding on the apparent horizon equation (York (1989))

$$H \equiv \frac{\partial_r B}{\sqrt{A} B} - 2 \frac{Y}{B} = 0 \quad (\text{B7})$$

[In detail, to locate apparent horizons we first search the grid function H for sign changes. For each sign change (distinct apparent horizon), we construct a local (Lagrange) interpolating polynomial for the H values in the manner of appendix F, then use the ZEROIN code of Forsythe *et al.* (1977), chapter 7, to locate the interpolating polynomial's zero.]

Note that in spherical symmetry any apparent horizon must have $r_{\text{areal}} = 2m$. [To see this,¹⁷ observe that in spherical symmetry, the Hawking mass function agrees with the Misner-Sharp one, and is given by $m_H = \frac{1}{2} r_{\text{areal}} (1 - \frac{1}{4} \omega_+ \omega_-)$, where ω_+ and ω_- are the null expansions, normalized to +2 in flat spacetime. An apparent horizon is defined by one or both of the expansions vanishing, so $m \equiv m_H = \frac{1}{2} r_{\text{areal}}$ there.]

¹⁷This argument was suggested to the author by N. Ó Murchadha.

2. Scalar Field Variables

The 3 + 1 energy and momentum densities are

$$4\pi\rho = \frac{1}{2}\frac{P^2}{A} + \frac{1}{2}Q^2 \quad (\text{B8})$$

$$4\pi j_i = \begin{bmatrix} -PQ & 0 & 0 \end{bmatrix} \quad (\text{B9})$$

$$4\pi j^i = \begin{bmatrix} -\frac{PQ}{A} & 0 & 0 \end{bmatrix} \quad (\text{B10})$$

and the spatial stress-energy tensor and its trace are

$$4\pi T_{ij} = \text{diag} \left[4\pi T_{rr} \quad 4\pi T_{\theta\theta} \quad 4\pi T_{\theta\theta} \sin^2 \theta \right] \quad (\text{B11})$$

$$4\pi T_{rr} = \frac{1}{2}P^2 + \frac{1}{2}AQ^2 \quad (\text{B12})$$

$$4\pi T_{\theta\theta} = -\frac{1}{2}\frac{B}{A}P^2 + \frac{1}{2}BQ^2 \quad (\text{B13})$$

$$4\pi T = -\frac{1}{2}\frac{P^2}{A} + \frac{3}{2}Q^2 \quad (\text{B14})$$

3. Constraints, Mass Functions, and 4-Invariants

The energy and momentum constraints are

$$C \equiv \left(R + 2\frac{Y^2}{B^2} + 4\frac{XY}{AB} \right) - \left(2\frac{P^2}{A} + 2Q^2 \right) = 0 \quad (\text{B15})$$

and

$$C^i = \begin{bmatrix} C^r & 0 & 0 \end{bmatrix} \quad (\text{B16})$$

$$C^r \equiv \left(-2\frac{\partial_r Y}{AB} + \frac{(\partial_r B)Y}{AB^2} + \frac{(\partial_r B)X}{A^2 B} \right) - \left(-2\frac{PQ}{A} \right) = 0 \quad (\text{B17})$$

In spherical symmetry the mass contained within a given radius is given by the Misner-Sharp mass function (Misner and Sharp (1964); Misner *et al.* (1973), section 23.5). As discussed in appendix C, for our purposes this is most usefully expressed in the form

$$m_{\text{MS}} = \frac{1}{2}\sqrt{B} \left(1 - \frac{1}{4}\frac{(\partial_r B)^2}{AB} + \frac{Y^2}{B} \right) \quad (\text{B18})$$

Notice that since $B \equiv g_{\theta\theta} = O(r^2)$, the leading term in (B18) is $O(r)$ for large r . For our slices m_{MS} is always $O(1)$ outside the scalar field shells, so the remaining terms in (B18) (must) nearly cancel the leading term. This cancellation, and thus our computation of m_{MS} , is thus quite sensitive to small finite differencing and roundoff errors at large r .

As discussed in section VIII, we thus use the integrated-scalar-field mass function m_μ defined by (13). Guven and Ó Murchadha (1995) define μ as

$$\mu = \left(\frac{\partial r_{\text{areal}}}{\partial \ell} \right) \rho - (r_{\text{areal}} K_{\theta}^{\theta}) j^r \quad (\text{B19})$$

where ℓ is the proper radial distance in the slice, i.e. $d\ell = \sqrt{g_{rr}} dr$. We thus have

$$\mu = \frac{1}{2} \frac{\partial_r B}{\sqrt{A}\sqrt{B}} \rho - \frac{\sqrt{A}}{\sqrt{B}} Y j^r \quad (\text{B20})$$

To actually calculate m_{μ} , we reformulate the integral (13) in terms of our nonuniform gridding coordinate w (cf. section VIII),

$$m_{\mu} = m_{\text{MS}}(r_{\text{min}}) + \int_{w_{\text{min}}}^w \frac{4\pi B \mu}{\partial w / \partial r} \sqrt{A} dw \quad (\text{B21})$$

then use the alternate form of Simpson's rule given by Press *et al.* (1986), (4.1.14), to do the numerical integration. (The standard form of Simpson's rule is inconvenient here because it only yields results at every 2nd grid point.)

As noted in section VIII, the 4-Ricci scalar is given by ${}^{(4)}R = 8\pi(\rho - T)$, so we have

$${}^{(4)}R = 2 \frac{P^2}{A} - 2Q^2 \quad (\text{B22})$$

We compute the 4-Riemann curvature invariant $R_{abcd}R^{abcd}$ via the general expression (14), using the subexpressions

$$K^i{}_k K^{kj} = \text{diag} \left[\frac{X^2}{A^2} \quad \frac{Y^2}{B^2} \quad \frac{Y^2}{B^2} \frac{1}{\sin^2 \theta} \right] \quad (\text{B23})$$

$$K_{ij} K^{jk} K_{kl} K^{li} = \frac{X^4}{A^4} + 2 \frac{Y^4}{B^4} \quad (\text{B24})$$

$$K_{ij} K^i{}_k K^{kj} = \frac{X^3}{A^3} + 2 \frac{Y^3}{B^3} \quad (\text{B25})$$

$$K_{ij} K^{ij} = \frac{X^2}{A^2} + 2 \frac{Y^2}{B^2} \quad (\text{B26})$$

The only nonzero components of $\nabla_i K_{jk}$ and $\nabla_{[i} K_{j]k}$ are

$$\nabla_r K_{rr} = \partial_r X - X \frac{\partial_r A}{A} \quad (\text{B27a})$$

$$\nabla_r K_{\theta\theta} = \partial_r Y - Y \frac{\partial_r B}{B} \quad (\text{B27b})$$

$$\nabla_r K_{\phi\phi} = \left[\partial_r Y - Y \frac{\partial_r B}{B} \right] \sin^2 \theta \quad (\text{B27c})$$

$$\nabla_{\theta} K_{r\theta} = \nabla_{\theta} K_{\theta r} = \frac{1}{2} \left(\frac{X}{A} - \frac{Y}{B} \right) \partial_r B \quad (\text{B27d})$$

$$\nabla_{\phi} K_{r\phi} = \nabla_{\phi} K_{\phi r} = \left[\frac{1}{2} \left(\frac{X}{A} - \frac{Y}{B} \right) \partial_r B \right] \sin^2 \theta \quad (\text{B27e})$$

and

$$\nabla_{[r}K_{\theta]\theta} = -\nabla_{[\theta}K_{r]\theta} = \partial_r Y - \frac{1}{2} \left(\frac{X}{A} + \frac{Y}{B} \right) \partial_r B \quad (\text{B28a})$$

$$\nabla_{[r}K_{\phi]\phi} = -\nabla_{[\phi}K_{r]\phi} = \left[\partial_r Y - \frac{1}{2} \left(\frac{X}{A} + \frac{Y}{B} \right) \partial_r B \right] \sin^2 \theta \quad (\text{B28b})$$

so that

$$\nabla_{[i}K_{j]k} \nabla^i K^{jk} = \frac{2}{AB^2} \left[\partial_r Y - \frac{1}{2} \left(\frac{X}{A} + \frac{Y}{B} \right) \partial_r B \right]^2 \quad (\text{B29})$$

4. York Decomposition Variables and Boundary Conditions

The terms and coefficients in the York equation (5) and its Jacobian (8) are

$$\nabla_i \nabla^i \Psi = \left(\frac{1}{A} \right) \partial_{rr} \Psi + \left(\frac{\partial_r B}{AB} - \frac{1}{2} \frac{\partial_r A}{A^2} \right) \partial_r \Psi \quad (\text{B30})$$

$$F_{ij} = \text{diag} \left[F_{rr} \quad -\frac{1}{2} \frac{B}{A} F_{rr} \quad -\frac{1}{2} \frac{B}{A} F_{rr} \sin^2 \theta \right] \quad (\text{B31})$$

$$F_{rr} = \left(\frac{2}{3} X - \frac{2}{3} \frac{A}{B} Y \right) + \left(\frac{2}{3} \partial_r A - \frac{2}{3} \frac{A}{B} \partial_r B \right) \partial_r \Omega + \left(\frac{4}{3} A \right) \Omega \quad (\text{B32})$$

$$F_{ij} F^{ij} = \frac{3}{2} \left(\frac{F_{rr}}{A} \right)^2 \quad (\text{B33})$$

$$(\Delta_\ell \Omega)^i = \text{diag} \left[(\Delta_\ell \Omega)^r \quad 0 \quad 0 \right] \quad (\text{B34})$$

$$\begin{aligned} (\Delta_\ell \Omega)^r &= \left(\frac{4}{3} \frac{1}{A} \right) \partial_{rr} \Omega + \left(\frac{2}{3} \frac{\partial_r A}{A^2} + \frac{4}{3} \frac{\partial_r B}{AB} \right) \partial_r \Omega \\ &\quad + \left(\frac{2}{3} \frac{\partial_{rr} A}{A^2} - \frac{2}{3} \frac{\partial_{rr} B}{AB} - \frac{2}{3} \frac{(\partial_r A)^2}{A^3} - \frac{1}{3} \frac{(\partial_r B)^2}{AB^2} + \frac{(\partial_r A)(\partial_r B)}{A^2 B} \right) \Omega \end{aligned} \quad (\text{B35})$$

$$(\ell \Omega)_{ij} = \text{diag} \left[(\ell \Omega)_{rr} \quad -\frac{1}{2} \frac{B}{A} (\ell \Omega)_{rr} \quad -\frac{1}{2} \frac{B}{A} (\ell \Omega)_{rr} \sin^2 \theta \right] \quad (\text{B36})$$

$$(\ell \Omega)_{rr} = \left(\frac{4}{3} A \right) \partial_r \Omega + \left(\frac{2}{3} \partial_r A - \frac{2}{3} \frac{A}{B} \partial_r B \right) \Omega \quad (\text{B37})$$

$$F_{ij} (\ell \Omega)^{ij} = \frac{3}{2} \frac{1}{A^2} F_{rr} (\ell \Omega)_{rr} \quad (\text{B38})$$

$$\nabla^i K = \text{diag} \left[\nabla^r K \quad 0 \quad 0 \right] \quad (\text{B39})$$

$$\nabla^r K = \frac{\partial_r X}{A^2} + 2 \frac{\partial_r Y}{AB} - \frac{X \partial_r A}{A^3} - 2 \frac{Y \partial_r B}{AB^2} \quad (\text{B40})$$

$$\nabla_j E^{ij} = \text{diag} \left[\nabla_j E^{rj} \quad 0 \quad 0 \right] \quad (\text{B41})$$

$$\nabla_j E^{rj} = \frac{2}{3} \frac{\partial_r X}{A^2} - \frac{2}{3} \frac{\partial_r Y}{AB} - \frac{2}{3} \frac{X \partial_r A}{A^3} - \frac{1}{3} \frac{Y \partial_r B}{AB^2} + \frac{X \partial_r B}{A^2 B} \quad (\text{B42})$$

In spherical symmetry, the outer boundary conditions (10a) and (11) become

$$\partial_r \Psi + \frac{\Psi - 1}{r} = O \left(\frac{1}{r^3} \right) \approx 0 \quad (\text{at } r = r_{\max}) \quad (\text{B43})$$

and

$$\partial_r \Omega + \frac{\Omega}{r} = O\left(\frac{1}{r^3}\right) \approx 0 \quad (\text{at } r = r_{\max}) \quad (\text{B44})$$

respectively.

APPENDIX C: THE MISNER-SHARP MASS FUNCTION IN SPHERICAL SYMMETRY

One of our major diagnostics is the Misner-Sharp mass function, which we use in the form (B18). Here we outline the derivation of this result.

Misner and Sharp (1964) gave the original derivation of the mass function for a spherically symmetric dynamic spacetime. However, their results [their equations (6.7) and (6.9)] aren't directly usable in a 3+1 code such as ours, for two reasons: First, their results are expressed in terms of Lagrangian-coordinate (comoving) matter variables, whereas we use Eulerian (non-comoving) coordinates. Second, their results are in the form of integrals from the origin out to a given radius (analogously to (13) but with lower limits of $r = 0$), whereas with the black hole exclusion technique the field variables aren't known (and in fact are generally singular) in the neighbourhood of the origin.

We thus begin instead with the (equivalent) alternate formulation of the Misner-Sharp mass function given by Misner *et al.* (1973), section 23.5,

$$m_{\text{MS}} = \frac{1}{2} \bar{r} \left(1 - \frac{1}{\bar{g}_{\bar{r}\bar{r}}} \right) \quad (\text{C1})$$

where the bars denote the use of Schwarzschild coordinates $\bar{x}^a = (\bar{t}, \bar{r}, \theta, \phi)$, defined by requiring the 4-metric to be diagonal ($\bar{g}_{\bar{t}\bar{r}} = 0$) and the radial coordinate to be areal ($\bar{g}_{\theta\theta} = \bar{r}^2$).

In our 3+1 code we permit the coordinates to be arbitrarily chosen (within the restriction of spherical symmetry), i.e. we permit the 4-metric to be non-diagonal and/or the radial coordinate to be non-areal. To transform (C1) back to such generic coordinates, we first define an intermediate coordinate system $\hat{x}^a = (t, \bar{r}, \theta, \phi)$, which uses our generic time coordinate t but retains the areal radial coordinate \bar{r} . From the requirement that $\bar{g}_{\bar{t}\bar{r}} = 0$, a straightforward calculation shows that $\bar{g}_{\bar{r}\bar{r}} = \hat{g}_{\bar{r}\bar{r}} - (\hat{g}_{t\bar{r}})^2 / \hat{g}_{tt}$, and hence

$$m_{\text{MS}} = \frac{1}{2} \bar{r} \left[1 - \frac{1}{\hat{g}_{\bar{r}\bar{r}}} + \left(\frac{\hat{\beta}}{\hat{\alpha}} \right)^2 \right] \quad (\text{C2})$$

[This result appears somewhat problematic, as it has m apparently depending on the freely specifiable \hat{x}^a -coordinate lapse and shift $\hat{\alpha}$ and $\hat{\beta}$. However, the areal radial coordinate condition $\hat{g}_{\theta\theta} = \bar{r}^2$ actually fixes the ratio $\hat{\beta}/\hat{\alpha}$ which enters into m (i.e. this ratio actually *isn't* freely specifiable), so there's no difficulty.]

From the requirement that $\hat{g}_{\theta\theta} = \bar{r}^2$ it then follows that $\partial r / \partial \bar{r} = 2\sqrt{B} / \partial_r B$, and hence

$$m_{\text{MS}} = \frac{1}{2} \sqrt{B} \left(1 - \frac{1}{4} \frac{(\partial_r B)^2}{AB} + \frac{Y^2}{B} \right) \quad (\text{C3})$$

which is the desired generic-coordinates form for the mass function.

APPENDIX D: NUMERICAL COORDINATE TRANSFORMATIONS

In 3 + 1 numerical relativity one often uses coordinate conditions which fix the form of the spatial metric. For example, one may wish to force the radial coordinate to be areal ($g_{\theta\theta} = r^2$). Even if our Ansatz for the base field variables satisfies such a condition, in general the York projection operator (4) doesn't preserve it. As the final step in our overall initial data algorithm (step 4 in our presentation of section VII), we thus optionally apply an explicit numerical coordinate transformation to the output of the York projection, so as to (e.g.) convert it back to an areal radial coordinate.

We actually use a numerical-coordinate-transformation algorithm somewhat more general than is needed just for this purpose: our algorithm actually applies a generic (nonsingular and invertible) numerically specified radial-coordinate transformation $r \rightarrow \tilde{r} = \tilde{r}(r)$. (To specify a transformation to an areal radial coordinate, we simply take $\tilde{r} = \sqrt{g_{\theta\theta}}$.)

Numerical coordinate transformations are conceptually straightforward, but somewhat complicated in detail due to the field variables only being known on the finite difference grid. In our case the use of the nonuniform gridding coordinate w further complicates matters. Figure 16 summarizes our numerical coordinate transformation algorithm; given this flowchart the operations involved should be self-evident. Notice that as well as tensor-transforming the field variables, the algorithm must also interpolate them from the r to the \tilde{r} grid. We use moving local (Lagrange) polynomial interpolation for this, as discussed in detail in appendix F.

APPENDIX E: CONVERGENCE TESTS

As discussed in section XIC, several different error sources are present in a 3 + 1 code such as ours, but the dominant one is usually finite differencing truncation error. As has been forcefully emphasized by Choptuik (1986, 1991); Choptuik *et al.* (1992), in such a situation a careful comparison of the errors in approximating the same physical system at different grid resolutions can yield a great deal of information about, and very stringent tests of, the code's numerical performance and correctness.

In the present context, consider some diagnostic Z whose true (continuum) value Z^* is known. [For example, the true values of the energy and momentum constraints C and C^i are zero, and in section XI E the true value of $I/I_{\text{Schw}(m_{\text{total}})}$ in the (vacuum) daw5 slice is 1, where $I \equiv R_{abcd}R^{abcd}$.] Suppose we have a pair of numerically computed approximate initial data slices, identical except for having a 2:1 ratio of grid spacings Δw . As discussed in detail by Choptuik (1991), if all the field variables are smooth and the code's numerical errors are dominated by truncation errors from n th order finite differencing, the numerically computed diagnostics Z must satisfy the Richardson expansion

$$Z[\Delta w] = Z^* + (\Delta w)^n f + O((\Delta w)^{n+2}) \tag{E1a}$$

$$Z[\Delta w/2] = Z^* + (\Delta w/2)^n f + O((\Delta w)^{n+2}) \tag{E1b}$$

at each grid point, where $Z[\Delta w]$ denotes the numerically computed Z using the grid spacing Δw , and f is an $O(1)$ smooth function depending on various high order derivatives of Z^* and the field variables, but *not* on the grid resolution. [We're assuming centered finite

differencing here in writing the higher order terms as $O((\Delta w)^{n+2})$, otherwise they would only be $O((\Delta w)^{n+1})$.] Neglecting the higher order terms, i.e. in the limit of small Δw , we can eliminate f to obtain a direct relationship between the code’s errors at the two resolutions,

$$\frac{Z[\Delta w/2] - Z^*}{Z[\Delta w] - Z^*} = \frac{1}{2^n} \tag{E2}$$

which must hold at each grid point common to the two grids.

We use two methods for testing how well or poorly any particular set of (finite-resolution) numerical results satisfies the convergence criterion (E2): One method, used here in figures 8, 11, 14, and 15, is to plot the absolute values of the low-resolution and high-resolution errors ($|Z[\Delta w] - Z^*|$ and $|Z[\Delta w/2] - Z^*|$ respectively) on a common *logarithmic* scale. If, and given the arguments of Choptuik (1991), in practice *only* if, the error expansions (E1) are valid with the higher order error terms negligible, i.e. if and only if the errors are indeed dominated by the expected n th order finite difference truncation errors, then the two curves will be identical except for the high-resolution curve being offset downwards (towards smaller errors) by a factor of 2^n from the low-resolution curve.

Our other method (Thornburg (1993, 1996)) for testing our results against the convergence criterion (E2), used here in figure 9, is to plot a scatterplot of the high-resolution errors $Z[\Delta w/2] - Z^*$ against the low-resolution errors $Z[\Delta w] - Z^*$ at the grid points common to the two grids. If, and again in practice *only* if, the error expansions (E1) are valid with the higher order error terms negligible, i.e. if and only if the errors are indeed dominated by the expected n th order finite difference truncation errors, then all the points in the scatterplot will fall on a line through the origin with slope $1/2^n$ ($= \frac{1}{16}$ for 4th order convergence).

Comparing these analyses, each has its advantages and disadvantages: The logarithmic analysis simultaneously tests the convergence criterion (E2), and gives a good qualitative overview of the overall magnitude and spatial variation of the errors. Moreover, the use of a logarithmic plot gives this method excellent dynamic range, i.e. it can easily test deviations from the convergence criterion in parts of the grid where the errors are small, even if elsewhere in the grid the errors are large. However, this analysis is relatively insensitive to small deviations from the expected convergence factor. In contrast, the scatterplot analysis has excellent sensitivity to small deviations from the expected convergence factor, but it doesn’t give any direct indication of where in the grid any problems lie, and it has limited dynamic range unless multiple plots at different scales are used (as in figure 9).

It’s important to note that both analyses are applied *pointwise*, i.e. independently at each grid point common to the two grids. This makes these analyses much more sensitive than a simple comparison of gridwise norms, which would tend to “wash out” any convergence problems occurring only in a small subset of the grid points (e.g. near a boundary).

[One “false alarm” problem of this type to which the scatterplot analysis is particularly subject, is that of boundary finite differencing effects: Near a grid boundary, we use off-centered molecules for finite differencing which, while still 4th order in accuracy, are an $O(1)$ factor less accurate than centered molecules we use in the grid interior. This in itself doesn’t cause a problem, but the choice of centered vs. off-centered molecules is based on the distance *in grid points* from the grid boundary, and so may differ at a near-boundary grid point between different-resolution grids. For example, with a 2:1 ratio of grid resolutions, a

point which is 2 grid points from the boundary (and thus can use a centered 5 point molecule) in the high-resolution grid, is only 1 grid point from the boundary (and thus must use an off-centered molecule) in the low-resolution grid. The different $O(1)$ factors in the different molecules' truncation errors then cause spurious apparent changes in the convergence ratios in (E2) at such grid points. This is the cause of the boundary artifacts in figures 8, 11, 14, and 15, and of the outlier points in figure 9.]

Finally, note that the parameter n , the order of the convergence, is (or at least should be) known in advance from the form of the finite differencing scheme. Thus the factor of 2^n convergence ratio in (E2), manifested in the vertical offset between the two plots in the logarithmic analysis, or in the slope of the line through the origin in the scatterplot analysis, isn't fitted to the data points, but is rather an a priori prediction with *no* adjustable parameters. A convergence test of either type is thus a very strong test of the validity of the overall finite differencing scheme and the error expansion (E1).

APPENDIX F: THE NON-SMOOTHNESS OF INTERPOLATION ERRORS

As discussed in appendix D, interpolation plays an important role in numerical coordinate transformation, and it's also important in horizon finding (Baumgarte *et al.* (1996); Thornburg (1996); Anninos *et al.* (1996); Huq (1996)). In this appendix we discuss some surprising properties of the errors in interpolation. For pedagogical convenience we focus only on (Lagrange) polynomial interpolation, but our results actually hold for a wide range of interpolation schemes.

To understand the behavior of interpolation errors, it's useful to consider an artificial example where the data being interpolated is in fact already known analytically: Suppose we have a smooth continuum function f and a set of grid points $\{x_k\}$ in its domain. To simplify our discussion we take the grid points $\{x_k\}$ to be uniformly spaced with spacing Δx , but again this restriction isn't essential.

Now define an interpolating function I using the function values $\{f(x_k)\}$ in the usual manner via an $n + 1$ point moving local interpolant: On each interval $[x_i, x_{i+1}]$ between adjacent grid points, we set I to the (unique) n th-degree interpolating polynomial $P[i]$ which agrees with the $\{f(x_k)\}$ values at the $n + 1$ nearest-neighbour grid points located symmetrically about the interval $[x_i, x_{i+1}]$.

Consider the interpolation error $e \equiv I - f$ in taking I as an approximation to f , and this error's behavior as the grid is refined ($\Delta x \rightarrow 0$). It's well known that for sufficiently smooth f , $e = O((\Delta x)^{n+1})$, so the error can be made small by refining the grid. But *the error function $e = e(x)$ is not smooth!* In fact, even if f is analytic, *the error function has a discontinuous (1st) derivative at each grid point.* This holds regardless of the interpolation order n .

The reason for this behavior is that although in any grid interval $[x_k, x_{k+1}]$, $I = P[k]$ is a smooth function (an n th-degree polynomial), I is a *different* such polynomial in each separate interval $[x_k, x_{k+1}]$. At each grid point the two adjacent interval's interpolating polynomials agree in their values (so I is continuous there), but not in their derivatives (so dI/dx and hence de/dx has a jump discontinuity there). In other words, e is a "bump function": it vanishes at each grid point, but between each pair of grid points it rises to a nonzero value, here with amplitude $O((\Delta x)^{n+1})$.

Now suppose we approximate derivatives of f by derivatives of the interpolating function I . Because of e 's non-smoothness, the Richardson-type argument outlined by Choptuik (1991) *doesn't* apply here. Instead, by considering the behavior of the interpolation process for polynomials f of varying degrees, it's straightforward to show that for the p th derivative the error in this approximation is

$$\frac{d^p e}{dx^p} \equiv \frac{d^p I}{dx^p} - \frac{d^p f}{dx^p} = O((\Delta x)^{n+1-p}) \quad (\text{F1})$$

Hence provided $p \leq n$, the error in approximating derivatives this way can still be made small by refining the grid, but due to the non-smoothness of the error function the effective order of convergence is lowered by the number of derivatives taken.

This analysis assumes that all differentiation (e.g. to compute $d^p I/dx^p$) is done exactly (analytically). However, if local numerical differentiation (finite differencing) is used instead, then it's easy to show that the error expansion (F1) still holds.

As an example of interpolation errors, consider the function f defined by $f(x) = \exp(\sin(\frac{\pi}{2}x))$, and take $n = 3$, so the local interpolation uses cubic polynomials fitted to 4 nearest-neighbour function values. Figure 17(a) shows the error e in this interpolation for grids with spacings in the 2:1 ratio $\Delta x = 0.1:0.05$, plotted for the range $[0, 0.5]$. (In each case the grids are enough larger than this range so the interpolations never encounter the grid endpoints.) The overall bump-function shape of the error is clearly evident, with e vanishing at the grid points (the interpolation is exact there), and rising to a maximum between each pair of grid points. The amplitudes of the ‘‘bumps’’ for the two grid spacings are in approximately a 16:1 ratio, confirming that we have 4th order convergence here, $e = O((\Delta x)^4)$.

Figure 17(b) shows the error de/dx in taking dI/dx as an approximation to df/dx for this same example. de/dx has a jump discontinuity at each grid point, corresponding to the abrupt change in slope going from one ‘‘bump’’ to the next in e (figure 17(a)). The amplitudes of de/dx for the two grid spacings are in approximately an 8:1 ratio, confirming that we only have 3rd order convergence here, $e = O((\Delta x)^3)$.

Our conclusion from this argument is that by virtue of (F1), if interpolated data is to be used as input to further finite differencing computations, then either the interpolation order should be raised sufficiently to compensate for the non-smoothness, or Hermite, spline, or other explicitly smoothness-preserving interpolation schemes should be used.

In our present computational scheme we use moving local polynomial interpolation in the manner described above. Our overall computational scheme is intended to be 4th order accurate, and we use numerical differentiation up to 2nd order (e.g. in the 3-Ricci tensor), so we use 5th order (Lagrange) polynomials for local interpolation in our numerical coordinate transformation and horizon finding algorithms. These interpolants give 6th order local truncation errors, so 2nd numerical derivatives of the interpolation results should still be 4th order accurate.

APPENDIX: REFERENCES

AbrahamsandEvans(1992) Abrahams, A. M. and Evans, C. R. (1992). Trapping a geon: Black hole formation by an imploding gravitational wave. *Physical Review D*, **46**(10), R4117–R4121.

- Anninos et al.*(1995) Anninos, P., Daues, G., Massó, J., Seidel, E., and Suen, W.-M. (1995). Horizon boundary condition for black hole spacetimes. *Physical Review D*, **51**(10), 5562–5578.
- Anninos et al.*(1996) Anninos, P., Camarda, K., Libson, J., Massó, J., Seidel, E., and Suen, W.-M. (1996). Finding apparent horizons in dynamic 3d numerical spacetimes.
- Arnowitt et al.*(1962) Arnowitt, R., Deser, S., and Misner, C. W. (1962). The dynamics of general relativity. In L. Witten, editor, *Gravitation: An Introduction to Current Research*, pages 227–265. Wiley, New York.
- Baumgarte et al.*(1996) Baumgarte, T. W., Cook, G. B., Scheel, M. A., Shapiro, S. L., and Teukolsky, S. A. (1996). Implementing an apparent-horizon finder in three dimensions. *Physical Review D*, **54**(8), 4849–4857.
- Bernstein and Bartnik*(1995) Bernstein, D. H. and Bartnik, R. (1995). A research in progress report on the evolution of spherically symmetric SU(2) Einstein-Yang-Mills fields. Technical report, University of New England (NSW, Australia).
- Bowen*(1979a) Bowen, J. M. (1979a). General form for the longitudinal momentum of a spherically symmetric source. *General Relativity and Gravitational*, **11**(3), 227–231.
- Bowen*(1979b) Bowen, J. M. (1979b). *Initial Value Problems on Non-Euclidean Topologies*. Ph.D. thesis, University of North Carolina at Chapel Hill.
- Bowen*(1982) Bowen, J. M. (1982). General solution for flat-space longitudinal momentum. *General Relativity and Gravitational*, **14**(12), 1183–1191.
- Bowen*(1985) Bowen, J. M. (1985). Inversion symmetric initial data for n charged black holes. *Annals of Physics*, **165**, 17–37.
- Bowen and York*(1980) Bowen, J. M. and York, Jr., J. W. (1980). Time-symmetric initial data for black holes and black hole collisions. *Physical Review D*, **21**(8), 2047–2056.
- Bowen et al.*(1984) Bowen, J. M., Rauber, J. D., and York, Jr., J. W. (1984). Two black holes with axisymmetric parallel spins: Initial data. *Classical and Quantum Gravity*, **1**, 591–610.
- Boyd*(1989) Boyd, J. P. (1989). *Chebyshev & Fourier Spectral Methods*, volume 49 of *Lecture Notes in Engineering*. Springer-Verlag, Berlin.
- Brill and Lindquist*(1963) Brill, D. R. and Lindquist, R. W. (1963). Interaction energy in geometrostatics. *Physical Review*, **131**(1), 471–476.
- Centrella et al.*(1986) Centrella, J. M., Shapiro, S. L., Evans, C. R., Hawley, J. F., and Teukolsky, S. A. (1986). Test-bed calculations in numerical relativity. In J. M. Centrella, editor, *Dynamical Spacetimes and Numerical Relativity*, pages 328–344. Cambridge University Press, Cambridge, UK. Proceedings of the Workshop on Dynamical Spacetimes and Numerical Relativity, Drexel University (Philadelphia, Pennsylvania, USA), 7–11 October 1985.

- Choptuik*(1982) Choptuik, M. W. (1982). *A Study of Numerical Techniques for the Initial Value Problem of General Relativity*. Master's thesis, University of British Columbia.
- Choptuik*(1986) Choptuik, M. W. (1986). *A Study of Numerical Techniques for Radiative Problems in General Relativity*. Ph.D. thesis, University of British Columbia.
- Choptuik*(1991) Choptuik, M. W. (1991). Consistency of finite-difference solutions of Einstein's equations. *Physical Review D*, **44**(10), 3124–3135.
- Choptuik et al.*(1992) Choptuik, M. W., Goldwirth, D. S., and Piran, T. (1992). A direct comparison of two codes in numerical relativity. *Classical and Quantum Gravity*, **9**, 721–750.
- Christoudolou*(1986a) Christoudolou, D. (1986a). *Communications in Mathematical Physics*, **105**, 337.
- Christoudolou*(1986b) Christoudolou, D. (1986b). *Communications in Mathematical Physics*, **106**, 587.
- Christoudolou*(1987a) Christoudolou, D. (1987a). *Communications in Mathematical Physics*, **109**, 591.
- Christoudolou*(1987b) Christoudolou, D. (1987b). *Communications in Mathematical Physics*, **109**, 613–647.
- Christoudolou*(1991) Christoudolou, D. (1991). The formation of black holes and singularities in spherically symmetric gravitational collapse. *Communications on Pure and Applied Mathematics*, **44**, 339–373.
- Christoudolou*(1993) Christoudolou, D. (1993). Bounded variation solutions of the spherically symmetric Einstein-scalar field equations. *Communications on Pure and Applied Mathematics*, **46**, 1131–1220.
- Cook*(1990) Cook, G. B. (1990). *Initial Data for the Two-Body Problem of General Relativity*. Ph.D. thesis, University of North Carolina at Chapel Hill.
- Cook*(1991) Cook, G. B. (1991). Initial data for axisymmetric black-hole collisions. *Physical Review D*, **44**(10), 2983–3000.
- Cook et al.*(1993) Cook, G. B., Choptuik, M. W., Dubal, M. R., Klasky, S., Matzner, R. A., and Oliveira, S. R. (1993). Three-dimensional initial data for the collision of two black holes. *Physical Review D*, **47**(4), 1471–1490.
- Dongarra et al.*(1979) Dongarra, J. J., Moler, C. B., Bunch, J. R., and Stewart, G. W. (1979). *LINPACK User's Guide*. Society for Industrial and Applied Mathematics, Philadelphia.
- Dubal*(1992) Dubal, M. R. (1992). Construction of three-dimensional black-hole initial data via multiquadrics. *Physical Review D*, **45**(4), 1178–1187.
- Dubal et al.*(1992) Dubal, M. R., Oliveira, S. R., and Matzner, R. A. (1992). Solution of elliptic equations in numerical relativity using multiquadrics. In R. d'Inverno, editor, *Approaches to Numerical Relativity*, pages 265–280. Cambridge University Press, Cambridge (UK). Proceedings of the International Workshop on Numerical Relativity, Southampton University (Southampton, England), 16–20 December 1991.

- EinsteinandRosen*(1935) Einstein, A. and Rosen, N. (1935). The particle problem in the general theory of relativity. *Physical Review*, **48**(10), 73–77.
- Forsythe et al.*(1977) Forsythe, G. E., Malcolm, M. A., and Moler, C. B. (1977). *Computer Methods for Mathematical Computations*. Prentice-Hall, Englewood Cliffs.
- GoldwirthandPiran*(1987) Goldwirth, D. S. and Piran, T. (1987). *Physical Review D*, **36**, 3575–3581.
- Goldwirth et al.*(1989) Goldwirth, D. S., Ori, A., and Piran, T. (1989). Cosmic censorship and numerical relativity. In C. R. Evans, L. S. Finn, and D. W. Hobill, editors, *Frontiers in Numerical Relativity*, pages 414–435. Cambridge University Press, Cambridge (UK). Proceedings of the International Workshop on Numerical Relativity, University of Illinois at Urbana-Champaign (Urbana-Champaign, Illinois, USA), 9–13 May 1988.
- Gómez et al.*(1996) Gómez, R., Laguna, P., Papadopoulos, P., and Winicour, J. (1996). Cauchy-characteristic evolution of Einstein-Klein-Gordon systems. *Physical Review D*, **54**(8), 4719–4727.
- GüvenandÓ Murchadha*(1995) Güven, J. and Ó Murchadha, N. (1995). The constraints in spherically symmetric classical general relativity: I. optical scalars, foliations, bounds on the configuration space variables, and the positivity of the quasilocal mass. *Physical Review D*, **52**(2), 758–775.
- HamadéandStewart*(1996) Hamadé, R. S. and Stewart, J. M. (1996). The spherically symmetric collapse of a massless scalar field. *Classical and Quantum Gravity*, **13**, 497–512.
- Huq*(1996) Huq, M. F. (1996). *Apparent Horizon Location in Numerical Spacetimes*. Ph.D. thesis, University of Texas at Austin.
- Isenberg*(1979) Isenberg, J. A. (1979). *The Construction of Spacetimes from Initial Data*. Ph.D. thesis, University of Maryland.
- Kulkarni*(1984a) Kulkarni, A. D. (1984a). Extrinsic curvature for the two-black-hole problem. *General Relativity and Gravitation*, **17**(4), 301–310.
- Kulkarni*(1984b) Kulkarni, A. D. (1984b). Time-asymmetric initial data for the n black hole problem in general relativity. *Journal of Mathematical Physics*, **25**(4), 1028–1034.
- Kulkarniet al.*(1983) Kulkarni, A. D., Shepley, L. C., and York, Jr., J. W. (1983). Initial data for n black holes. *Physics Letters*, **96A**(5), 228–230.
- Marsa*(1995) Marsa, R. L. (1995). *Radiative Problems in Black Hole Spacetimes*. Ph.D. thesis, University of Texas at Austin.
- MarsaandChoptuik*(1996) Marsa, R. L. and Choptuik, M. W. (1996). Black hole–scalar field interactions in spherical symmetry. *Physical Review D*, **54**(8), 4929–4943.
- Matzner et al.*(1998) Matzner, R. A., Huq, M. F., and Shoemaker, D. (1998). Initial data and coordinates for multiple black hole systems.

- Misner*⁽¹⁹⁶⁰⁾ Misner, C. W. (1960). Wormhole initial conditions. *Physical Review*, **118**(4), 1110–1111.
- MisnerandSharp*⁽¹⁹⁶⁴⁾ Misner, C. W. and Sharp, D. H. (1964). Relativistic equations for adiabatic, spherically symmetric gravitational collapse. *Physical Review B*, **136**(2), 571–576.
- Misner et al.*⁽¹⁹⁷³⁾ Misner, C. W., Thorne, K. S., and Wheeler, J. A. (1973). *Gravitation*. W. H. Freeman, San Francisco.
- Ó Murchadha*⁽¹⁹⁹²⁾ Ó Murchadha, N. (1992). Boundary conditions for the momentum constraint. In R. d’Inverno, editor, *Approaches to Numerical Relativity*, pages 83–93. Cambridge University Press, Cambridge (UK). Proceedings of the International Workshop on Numerical Relativity, Southampton University (Southampton, England), 16–20 December 1991.
- Ó MurchadhaandYork*^(1974a) Ó Murchadha, N. and York, Jr., J. W. (1974a). Initial-value problem of general relativity: I – general formulation and physical interpretation. *Physical Review D*, **10**(2), 428–436.
- Ó MurchadhaandYork*^(1974b) Ó Murchadha, N. and York, Jr., J. W. (1974b). Initial-value problem of general relativity: II – stability of solutions of the initial-value equations. *Physical Review D*, **10**(2), 437–446.
- OoharaandNakamura*⁽¹⁹⁸⁹⁾ Oohara, K. and Nakamura, T. (1989). Three dimensional initial data of numerical relativity. In C. R. Evans, L. S. Finn, and D. W. Hobill, editors, *Frontiers in Numerical Relativity*, pages 74–88. Cambridge University Press, Cambridge (UK). Proceedings of the International Workshop on Numerical Relativity, University of Illinois at Urbana-Champaign (Urbana-Champaign, Illinois, USA), 9–13 May 1988.
- Press et al.*⁽¹⁹⁸⁶⁾ Press, W. H., Flannery, B. P., Teukolsky, S. A., and Vetterling, W. T. (1986). *Numerical Recipes: The Art of Scientific Computing*. Cambridge University Press, Cambridge (UK) and New York, 1st edition.
- Rauber*⁽¹⁹⁸⁵⁾ Rauber, J. D. (1985). *Initial Data for Black Hole Collisions*. Ph.D. thesis, University of North Carolina at Chapel Hill.
- Rauber*⁽¹⁹⁸⁶⁾ Rauber, J. D. (1986). Initial data for black hole collisions. In J. M. Centrella, editor, *Dynamical Spacetimes and Numerical Relativity*, pages 304–327. Cambridge University Press, Cambridge, UK. Proceedings of the Workshop on Dynamical Spacetimes and Numerical Relativity, Drexel University (Philadelphia, Pennsylvania, USA), 7–11 October 1985.
- Scheel et al.*^(1995a) Scheel, M. A., Shapiro, S. L., and Teukolsky, S. A. (1995a). Collapse to black holes in Brans-Dicke theory: I. horizon boundary conditions for dynamical spacetimes. *Physical Review D*, **51**, 4208–4235.
- Scheel et al.*^(1995b) Scheel, M. A., Shapiro, S. L., and Teukolsky, S. A. (1995b). Collapse to black holes in Brans-Dicke theory: II. comparison with general relativity. *Physical Review D*, **51**, 4236.

- Scheel et al.*(1997) Scheel, M. A., Baumgarte, T. W., Cook, G. B., Shapiro, S. L., and Teukolsky, S. A. (1997). Numerical evolution of black holes with a hyperbolic formulation of general relativity. *Physical Review D*, **56**(10), 6320–6335.
- Seidel and Suen*(1992) Seidel, E. and Suen, W.-M. (1992). Towards a singularity-proof scheme in numerical relativity. *Physical Review Letters*, **69**(13), 1845–1848.
- Shapiro and Teukolsky*(1986) Shapiro, S. L. and Teukolsky, S. A. (1986). Relativistic stellar dynamics on the computer. In J. M. Centrella, editor, *Dynamical Spacetimes and Numerical Relativity*, pages 74–100. Cambridge University Press, Cambridge, UK. Proceedings of the Workshop on Dynamical Spacetimes and Numerical Relativity, Drexel University (Philadelphia, Pennsylvania, USA), 7–11 October 1985.
- Smarr*(1984) Smarr, L. L. (1984). Computational relativity: Numerical and algebraic approaches (report of workshop A4). In B. Bertotti, F. de Felice, and A. Pascolini, editors, *General Relativity and Gravitation: Invited Papers and Discussion Reports of the 10th International Conference on General Relativity and Gravitation, Padua, July 3–8 1983*, pages 163–183. Reidel, Dordrecht (Netherlands).
- Thornburg*(1985) Thornburg, J. (1985). *Coordinates and Boundary Conditions for the General Relativistic Initial Data Problem*. Master’s thesis, University of British Columbia.
- Thornburg*(1987) Thornburg, J. (1987). Coordinates and boundary conditions for the general relativistic initial data problem. *Classical and Quantum Gravity*, **4**, 1119–1131.
- Thornburg*(1991) Thornburg, J. (1991). Numerical relativity in black hole spacetimes.
- Thornburg*(1993) Thornburg, J. (1993). *Numerical Relativity in Black Hole Spacetimes*. Ph.D. thesis, University of British Columbia.
- Thornburg*(1996) Thornburg, J. (1996). Finding apparent horizons in numerical relativity. *Physical Review D*, **54**(8), 4899–4918.
- Thornburg*(1998) Thornburg, J. (1998). A 3 + 1 computational scheme for spherically symmetric dynamic black hole spacetimes – II: Time evolution. in preparation, to be submitted to *Physical Review D*.
- Wald*(1984) Wald, R. M. (1984). *General Relativity*. University of Chicago Press, Chicago.
- York*(1971) York, Jr., J. W. (1971). Gravitational degrees of freedom and the initial-value problem. *Physical Review Letters*, **26**(26), 1656–1658.
- York*(1972) York, Jr., J. W. (1972). Role of conformal three-geometry in the dynamics of gravitation. *Physical Review Letters*, **28**(16), 1082–1085.
- York*(1973) York, Jr., J. W. (1973). Conformally invariant orthogonal decomposition of symmetric tensors on Riemannian manifolds and the initial value problem of general relativity. *Journal of Mathematical Physics*, **14**(4), 456–464.

- York*⁽¹⁹⁷⁹⁾ York, Jr., J. W. (1979). Kinematics and dynamics of general relativity. In L. L. Smarr, editor, *Sources of Gravitational Radiation*, pages 83–126. Cambridge University Press, Cambridge, UK.
- York*⁽¹⁹⁸⁰⁾ York, Jr., J. W. (1980). Energy and momentum of the gravitational field. In F. J. Tipler, editor, *Essays in General Relativity: A Festschrift for Abraham Taub*, pages 39–58. Academic Press, New York.
- York*⁽¹⁹⁸³⁾ York, Jr., J. W. (1983). The initial value problem and dynamics. In N. Deruelle and T. Piran, editors, *Gravitational Radiation*, pages 175–201. North-Holland, Amsterdam.
- York*⁽¹⁹⁸⁴⁾ York, Jr., J. W. (1984). Initial data for n black holes. *Physica A*, **124**, 629–638.
- York*⁽¹⁹⁸⁵⁾ York, Jr., J. W. (1985). Spacetime engineering. In J. M. Centrella, J. M. LeBlanc, and R. L. Bowers, editors, *Numerical Astrophysics*, pages 176–189. Jones and Bartlett, Boston.
- York*⁽¹⁹⁸⁹⁾ York, Jr., J. W. (1989). Initial data for collisions of black holes and other gravitational miscellany. In C. R. Evans, L. S. Finn, and D. W. Hobill, editors, *Frontiers in Numerical Relativity*, pages 89–109. Cambridge University Press, Cambridge (UK). Proceedings of the International Workshop on Numerical Relativity, University of Illinois at Urbana-Champaign (Urbana-Champaign, Illinois, USA), 9–13 May 1988.
- YorkandPiran*⁽¹⁹⁸²⁾ York, Jr., J. W. and Piran, T. (1982). The initial value problem and beyond. In R. A. Matzner and L. C. Shepley, editors, *Spacetime and Geometry: The Alfred Schild Lectures*, pages 147–176. University of Texas Press, Austin (Texas).

FIG. 1. This figure shows the behavior of our nonuniform gridding coordinate w . Part (a) shows the grid spacing Δr for grids with resolutions of (top to bottom) $\Delta w = 0.01$, 0.005 , and 0.0025 . The diagonal dashed lines labeled along the top and right of the figure show lines of constant relative grid spacing $\Delta r/r$. Part (b) shows the actual w coordinate. In both parts of the figure the vertical dashed lines show the outer grid boundaries for $w_{\max} = 4$, 10 , and 30 .

FIG. 2. This figure shows the York-transformation conformal factor Ψ and vector potential Ω for the 200.pqw5 slice. The vertical dashed line at $r_{\text{init}} = 2$ shows the input horizon position.

FIG. 3. This figure shows the relative 3-metric and extrinsic curvature components $A \equiv g_{rr}$, $B \equiv g_{\theta\theta}$, $X \equiv K_{rr}$, and $Y \equiv K_{\theta\theta}$, for the 200.pqw5 slice. (Note that $B/B_{\text{Schw}} \equiv 1$ by the definition of an areal radial coordinate.) The vertical dashed line just inside $r = 2$ shows the horizon position.

FIG. 4. This figure shows the relative 3-invariants K , R , and $J \equiv R_{ij}R^{ij}$, for the 200.pqw5 slice. The horizontal dashed line shows the “zero axis” $K/K_{\text{Schw}} = R/R_{\text{Schw}} = J/J_{\text{Schw}} = 1$. The vertical dashed line just inside $r = 2$ shows the horizon position.

FIG. 5. This figure shows the scalar field and mass distributions for the 200.pqw5 slice. Part (a) shows the full data range, with logarithmic scales for most of the variables, while part (b) shows only the inner part of the grid, with linear scales for all variables. (In part (b) the left axis uses a different scale for $|{}^{(4)}R|$ than for $4\pi B\rho$ and $|P|$). In both parts of the figure the vertical dashed line just inside $r = 2$ shows the horizon position.

FIG. 6. This figure shows the mass-relative 4-Riemann curvature invariant $I \equiv R_{abcd}R^{abcd}$ for the 200.pqw5 slice. The vertical dashed line just inside $r = 2$ shows the horizon position. Notice that to within the accuracy of the plot, $I/I_{\text{Schw}(m(r))} = 1$ everywhere outside the scalar field shell.

FIG. 7. This figure shows the mass-relative 3-invariants K , R , and $J \equiv R_{ij}R^{ij}$, for the 200.pqw5 slice. The upper and lower horizontal dashed lines show the “zero axes” $K/K_{\text{Schw}(m(r))} = 1$ (left scale) and $R/R_{\text{Schw}(m(r))} = J/J_{\text{Schw}(m(r))} = 1$ (right scale) respectively. The vertical dashed line just inside $r = 2$ shows the horizon position.

FIG. 8. This figure shows the magnitudes of the numerically computed energy constraint C (part (a)), and momentum constraint C^r (part (b)), at various points in our initial data algorithm for the 100.pqw5 and 200.pqw5 slices. $|C_{\text{Schw}}|$ ($|C_{\text{Schw}}^r|$) is the magnitude of the energy (momentum) constraint of the initial Schwarzschild slice before applying the perturbation (step 1 in our overall initial data algorithm of section VII); $|C_{\text{perturb}}|$ ($|C_{\text{perturb}}^r|$) is the magnitude of the energy (momentum) constraint after applying the perturbation (step 2); and $|C_{\text{final}}|$ ($|C_{\text{final}}^r|$) is the magnitude of the final energy (momentum) constraint after applying the York algorithm (step 3) and the numerical coordinate transformation back to an areal radial coordinate (step 4). The scale bars show a factor of 16 in $|C|$ ($|C^r|$), for comparison with the vertical spacing between the 100.pqw5 and 200.pqw5 curves. For the 200.pqw5 $|C_{\text{perturb}}|$ curve, only every 5th grid point is plotted.

FIG. 9. This figure shows a scatterplot of C_{final} between the 100.pqw5 and 200.pqw5 slices. Part (a) shows all the C_{final} values, while part (b) shows an expanded view of the central region (the grid-interior points) of part (a). In each part the line through the origin has slope $\frac{1}{16}$; As discussed in appendix E, for 4th order convergence we expect all the points (except for grid-boundary outliers) to fall on the line.

FIG. 10. This figure shows various embedding and curvature diagnostics for the outermost part of the grid in the 100o30.pqw5 slice (part (a)), and the 200o30.pqw5 slice (part (b)). Each part of the figure shows the relative K ; the mass-relative $J \equiv R_{ij}R^{ij}$ and $I \equiv R_{abcd}R^{abcd}$; the relative R ; and the relative R_{fit} (an empirical least-squares fit to R) perturbed by simulated roundoff errors in the 3-metric components, with $\varepsilon = 6 \times 10^{-19}$. One outlier point in part (b), that for R/R_{Schw} at the outermost grid point, falls outside the plot's range and is omitted. (This point is anomalous due to boundary finite differencing effects.) Note that the plot key (the choice of line and point types used for the different diagnostics) differs between this and the other figures.

FIG. 11. This figure shows the magnitude of the numerically computed energy constraint, $|C|$, at various points in our initial data algorithm for the 100.pqw5i and 200.pqw5i slices, analogously to figure 8(a) for the 100.pqw5 and 200.pqw5 slices. $|C_{\text{Schw}}|$ is the magnitude of the energy constraint of the initial Schwarzschild slice before applying the perturbation (step 1 in our overall initial data algorithm of section VII); $|C_{\text{perturb}}|$ is the magnitude of the energy constraint after applying the perturbation (step 2), and $|C_{\text{final}}|$ is the magnitude of the final energy constraint after applying the York algorithm (step 3) and the numerical coordinate transformation back to an areal radial coordinate (step 4). The scale bar shows a factor of 16 in $|C|$, for comparison with the vertical spacing between the 100.pqw5i and 200.pqw5i curves. For the 200.pqw5i $|C_{\text{perturb}}|$ curve, only every 5th grid point is plotted.

FIG. 12. This figure shows the scalar field and mass distributions for the 200.pqw5b (part (a)) and 200.pqw5c (part (b)) slices, analogously to figure 5(a) for the 200.pqw5 slice. In both parts of the figure the left scale is identical to that of figure 5(a); the right scale differs for each part. In part (a) the vertical dashed line just inside $r = 2$ shows the horizon position. (As discussed in the text, there is no horizon within the numerical grid in the 200.pqw5c slice plotted in part (b).)

FIG. 13. This figure shows the scalar field and mass distributions for the 400.pqw1 slice, analogously to figure 5(a) for the 200.pqw5 slice and figure 12 for the 200.pqw5b and 200.pqw5c slices. Part (a) shows the full data range, while part (b) shows only the inner part of the grid. In both parts of the figure the vertical dashed line just inside $r = 2$ shows the horizon position.

FIG. 14. This figure shows the relative deviation $|m_{\text{MS}}/m_{\mu} - 1|$ of the Misner-Sharp mass function m_{MS} from the integrated-scalar-field mass function m_{μ} , for the 100.pw5+qw3 and 200.pw5+qw3 slices. The scale bar shows a factor of 16 in the deviations, for comparison with the vertical spacing between the 100.pw5+qw3 and 200.pw5+qw3 curves. The vertical dashed line just inside $r = 2$ shows the horizon position.

FIG. 15. This figure shows the relative errors $|m_{\text{MS}}/m_{\text{total}} - 1|$ and $|I/I_{\text{Schw}(m_{\text{total}})} - 1|$ in the Misner-Sharp mass function m_{MS} and the 4-Riemann curvature invariant $I \equiv R_{abcd}R^{abcd}$, for the 100.daw5c and 200.daw5c slices, where m_{total} is the total mass of the slice. The scale bar shows a factor of 16 in the errors, for comparison with the vertical spacing between the 100.daw5c and 200.daw5c curves. The vertical dashed line just outside $r = 2$ shows the horizon position.

FIG. 16. This figure shows the overall data flow in our numerical coordinate transformation algorithm. Oval boxes denote grid functions, rectangular boxes denote operations performed on grid functions, solid arrows show data flows presently used in our algorithm, and the dashed arrow shows an additional data flow which would be needed to transform contravariant tensors in addition to covariant ones. $f @ w$ and $f @ \tilde{w}$ denote a grid function f defined on the w and \tilde{w} grids respectively.

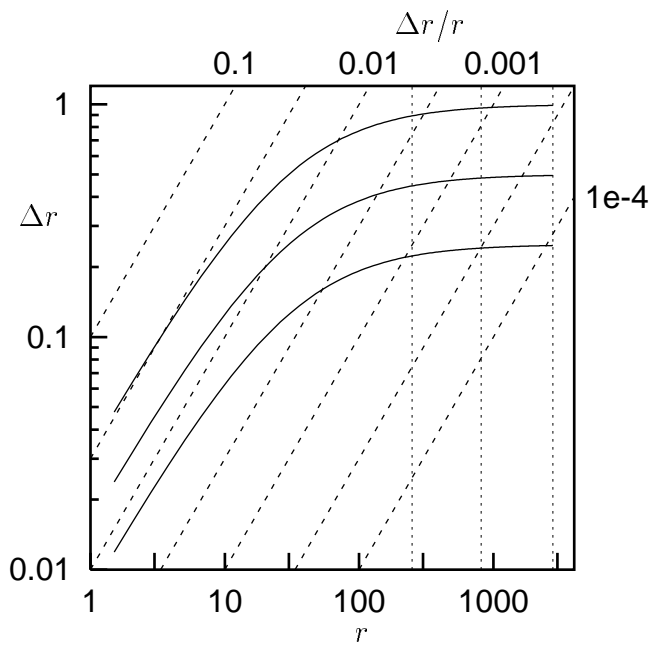
FIG. 17. This figure shows the interpolation error $e \equiv I - f$ (part (a)) and its derivative $de/dx \equiv dI/dx - df/dx$ (part (b)), for the function f defined by $f(x) = \exp(\sin(\frac{\pi}{2}x))$, cubically interpolated to grids with spacings $\Delta x = 0.1$ and 0.05 . The plot key for part (a) also applies to part (b).

TABLE I. This table gives various parameters for our test initial data slices. For each slice the table shows a descriptive name, the spatial grid resolution and size, the initial perturbation (step 2 in our overall initial data algorithm of section VII), an approximate Gaussian fit to the slice’s radial scalar field density $4\pi B\rho$, the horizon’s areal radius, and a summary of the slice’s mass distribution (broken down into black hole, scalar field, and total mass).

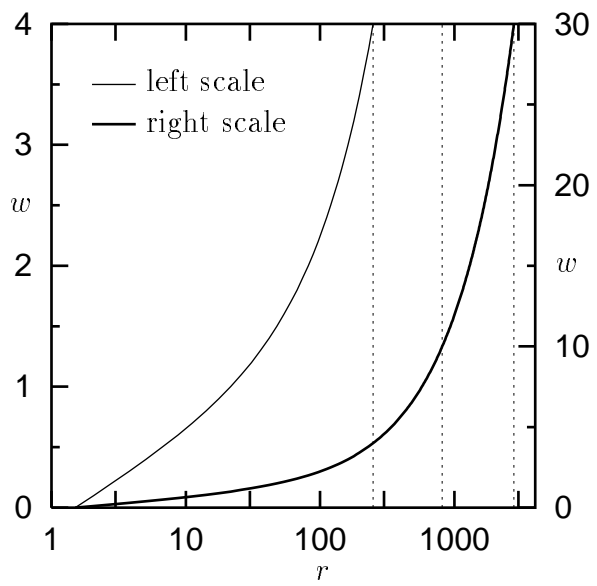
Name	Δw	$\Delta r/r$		w_{\max}	r_{\max}	Initial Perturbation	Approximate Pro Scalar Field Shell
		at $r=20$					
100.pqw5	0.01	0.02	}	4	248	$P \rightarrow P + 0.02 \times \text{Gaussian}(r_{\text{init}}=20, \sigma=5)$	$0.0735 \times \text{Gaussian}(r=21)$
200.pqw5	0.005	0.01					
100o10.pqw5	0.01	0.02					
200o10.pqw5	0.005	0.01	}	10	813		
100o30.pqw5	0.01	0.02					
200o30.pqw5	0.005	0.01	}	30	2780		
100.pqw5i	0.01	0.02				}	4
200.pqw5i	0.005	0.01					
100.pqw5b	0.01	0.02	}	4	248	$P \rightarrow P + 0.05 \times \text{Gaussian}(r_{\text{init}}=20, \sigma=5)$	$0.0365 \times \text{Gaussian}(r=24)$
200.pqw5b	0.005	0.01					
100.pqw5c	0.01	0.02	}	4	248	$P \rightarrow P + 0.1 \times \text{Gaussian}(r_{\text{init}}=20, \sigma=5)$	$0.91 \times \text{Gaussian}(r=31)$
200.pqw5c	0.005	0.01					
200.pqw1	0.005	0.01	}	4	248	$P \rightarrow P + 0.1 \times \text{Gaussian}(r_{\text{init}}=20, \sigma=1)$	$1.42 \times \text{Gaussian}(r=22)$
400.pqw1	0.0025	0.005					
100.pw5+qw3	0.01	0.02	}	4	248	$\left[P \rightarrow P + 0.02 \times \text{Gaussian}(r_{\text{init}}=20, \sigma=5) \right]^b$	$0.225 \times \text{Gaussian}(r=22)$
200.pw5+qw3	0.005	0.01					
100.daw5c	0.01	0.02	}	4	248	$A \rightarrow A + 0.1 \times \text{Gaussian}(r_{\text{init}}=20, \sigma=5)$	none
200.daw5c	0.005	0.01					

^aAs discussed in the text in section XI E, there’s no apparent horizon within this slice’s numerical grid; the “black hole” mass shown (within parentheses) is actually the mass within the inner grid boundary.

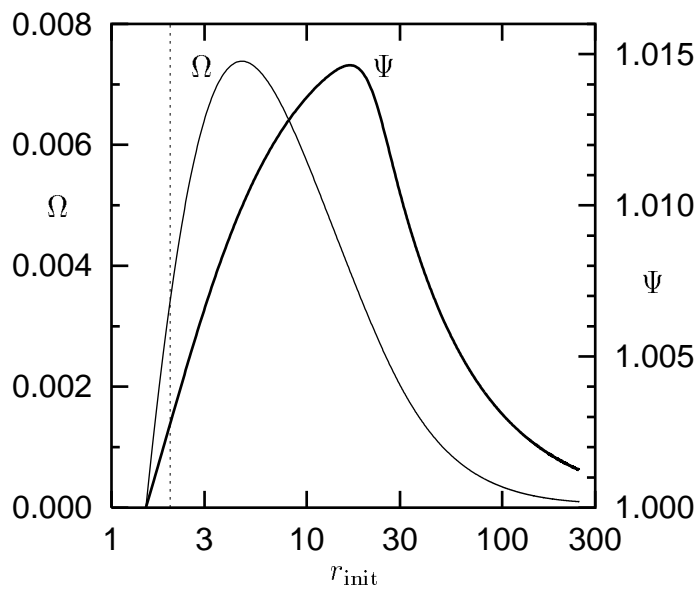
^bThe initial perturbation is to both P and Q for this slice.



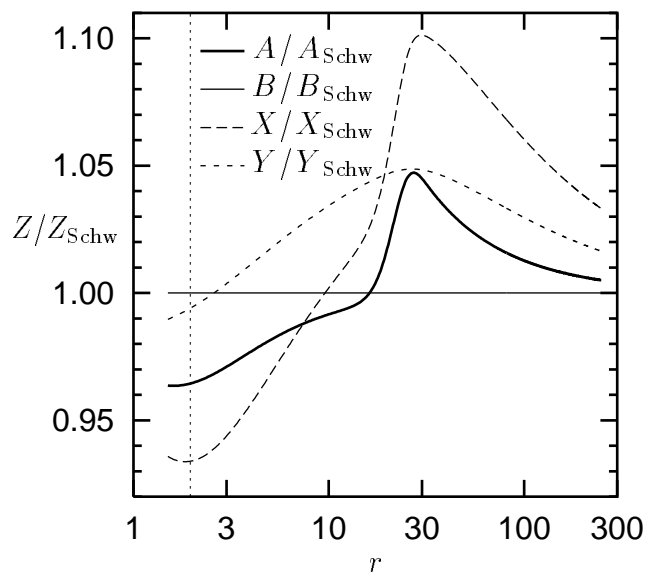
Thornburg Figure 1(a)



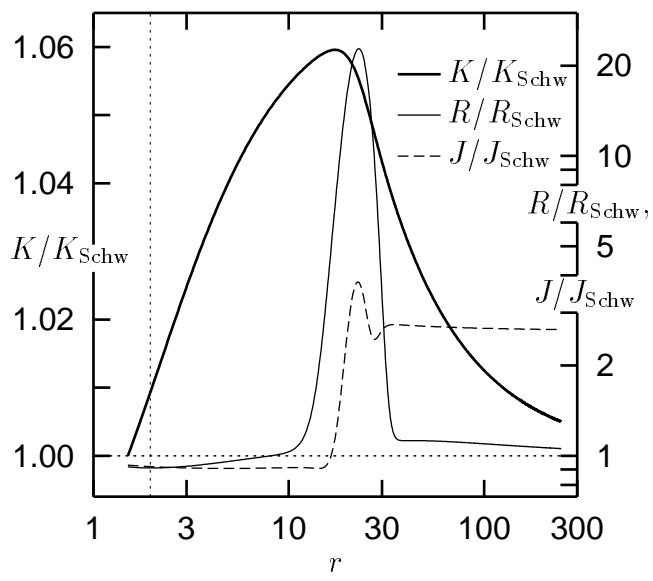
Thornburg Figure 1(b)



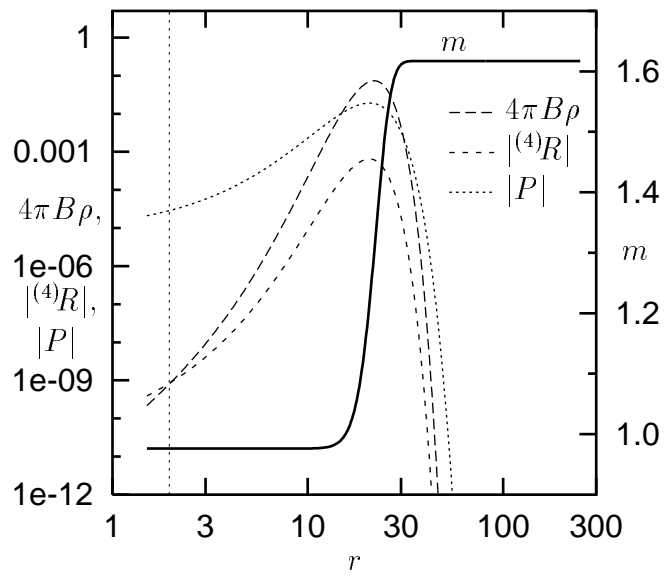
Thornburg Figure 2



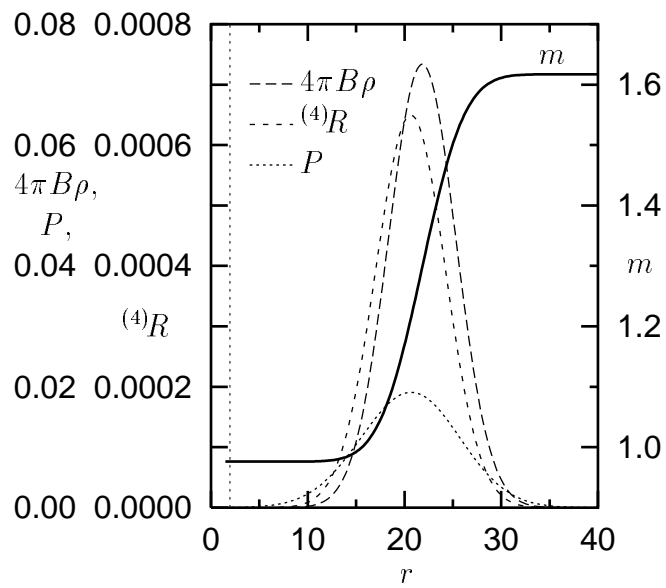
Thornburg Figure 3



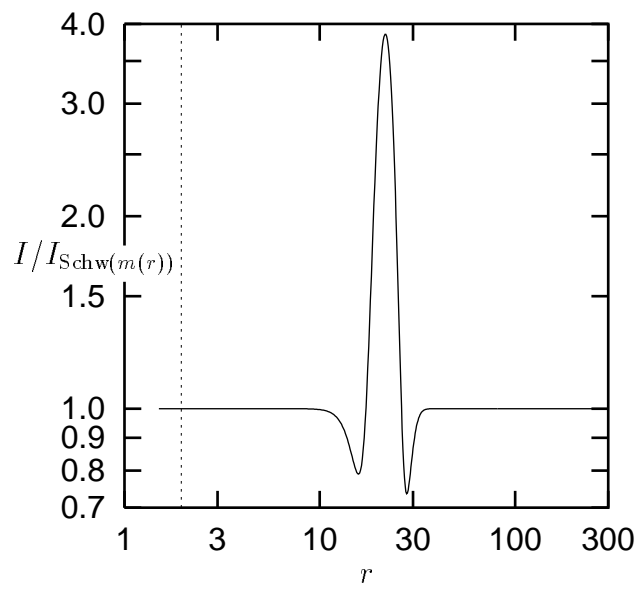
Thornburg Figure 4



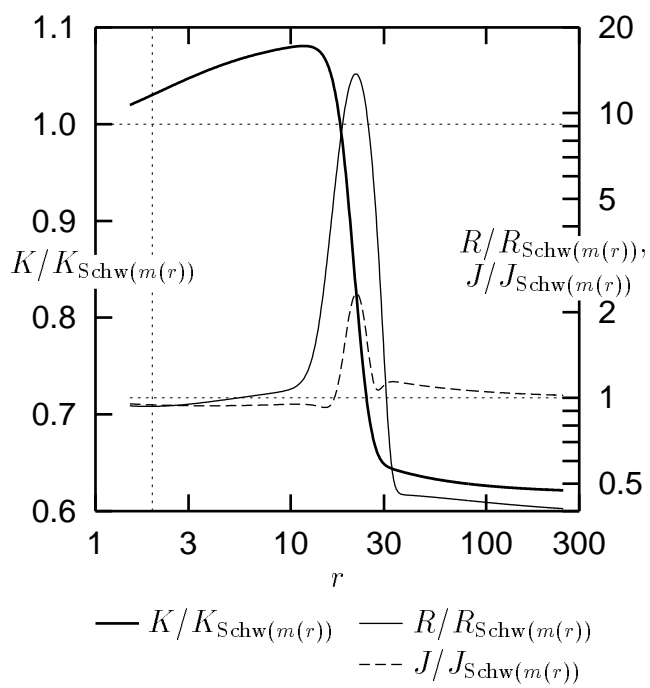
Thornburg Figure 5(a)



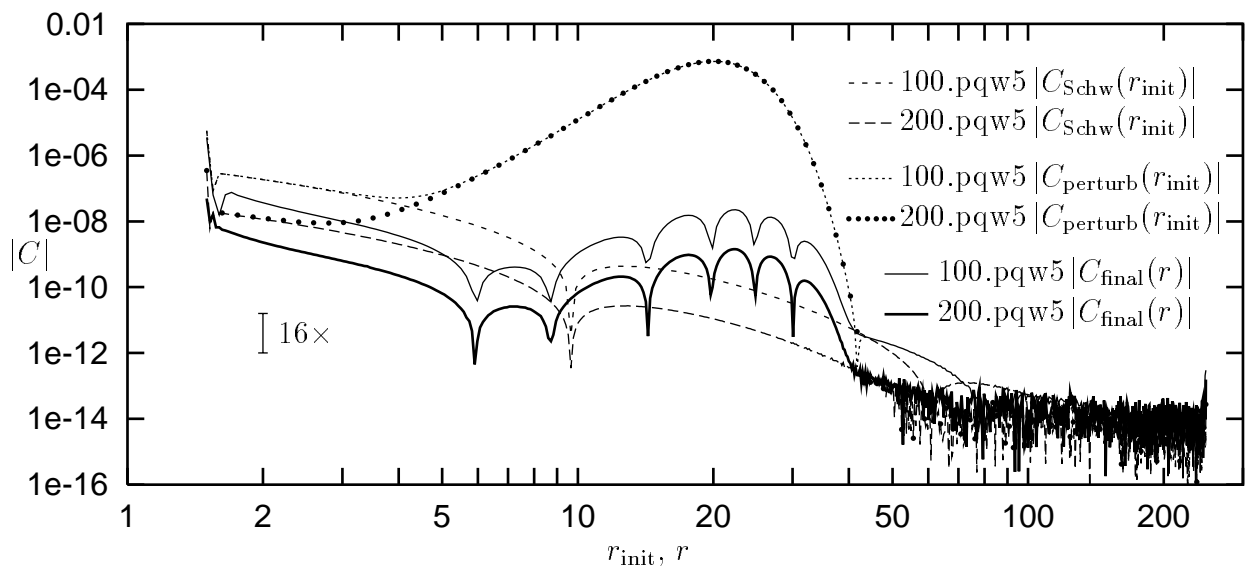
Thornburg Figure 5(b)



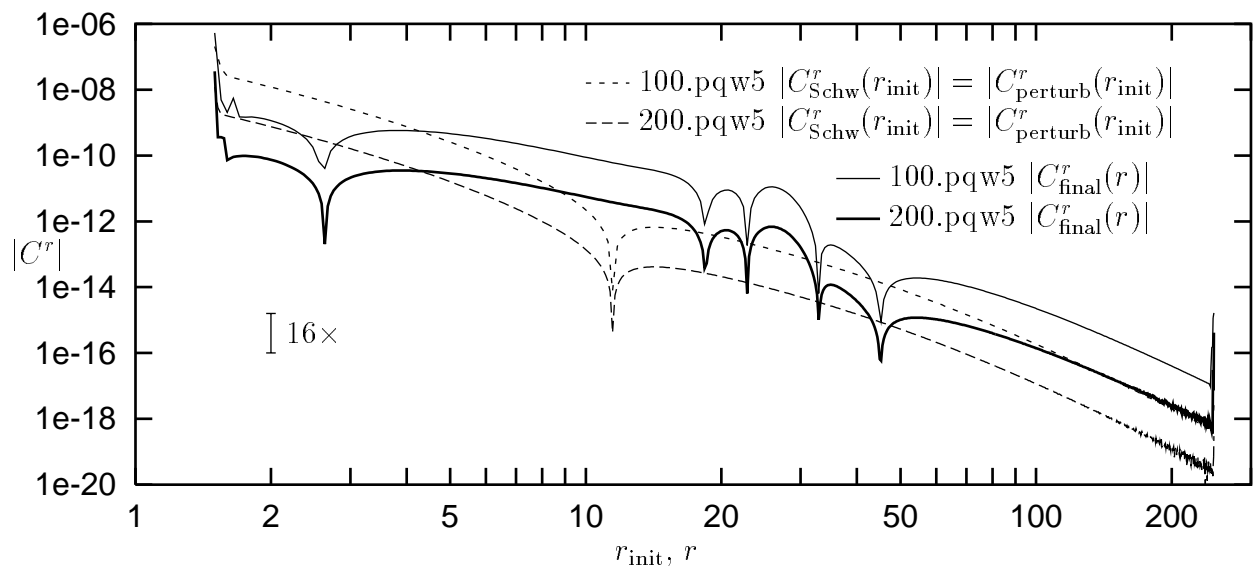
Thornburg Figure 6



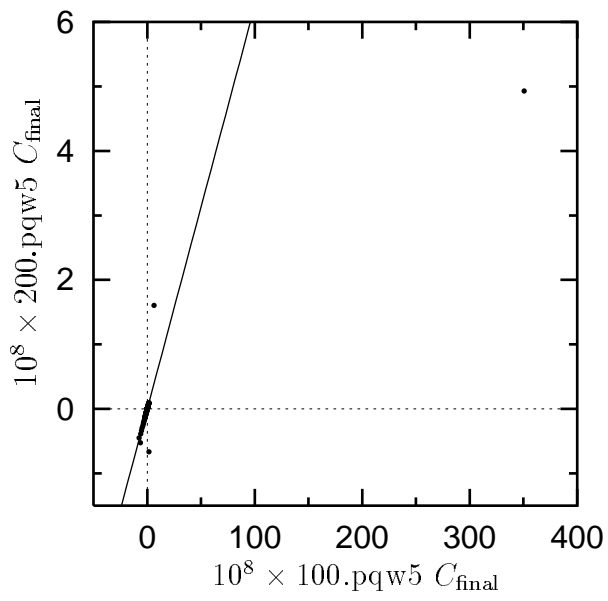
Thornburg Figure 7



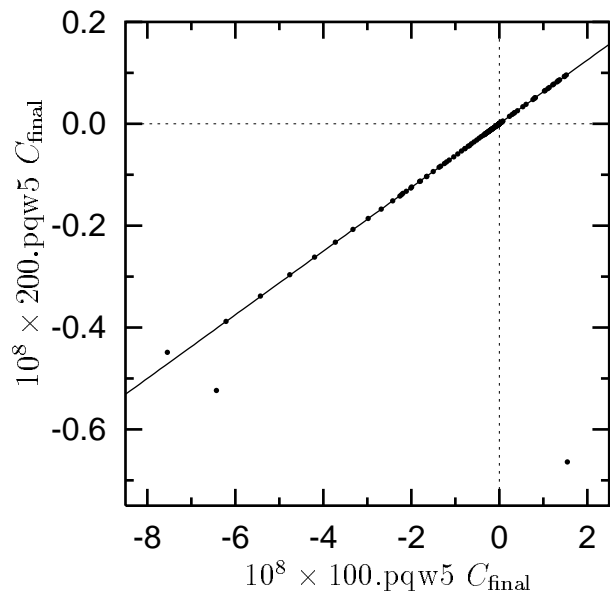
Thornburg Figure 8(a)



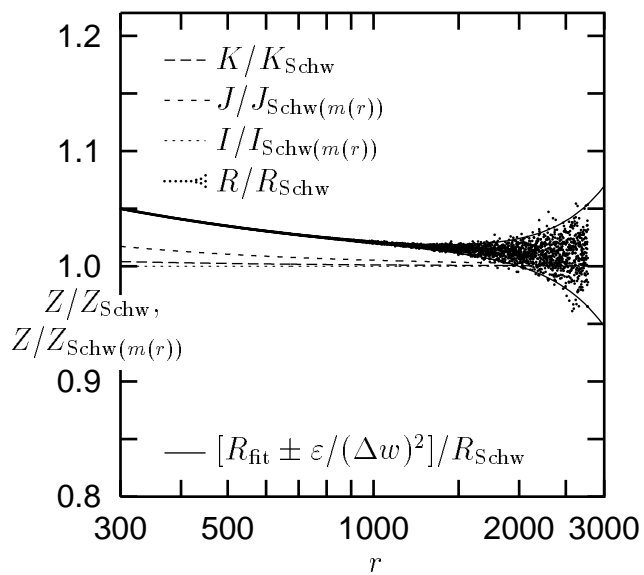
Thornburg Figure 8(b)



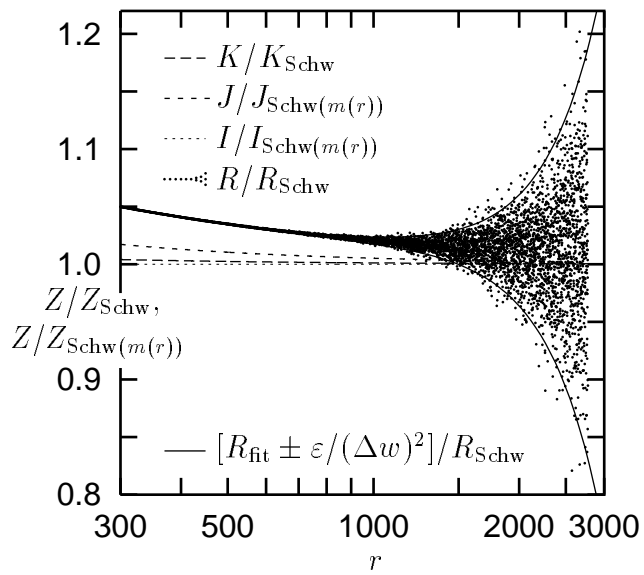
Thornburg Figure 9(a)



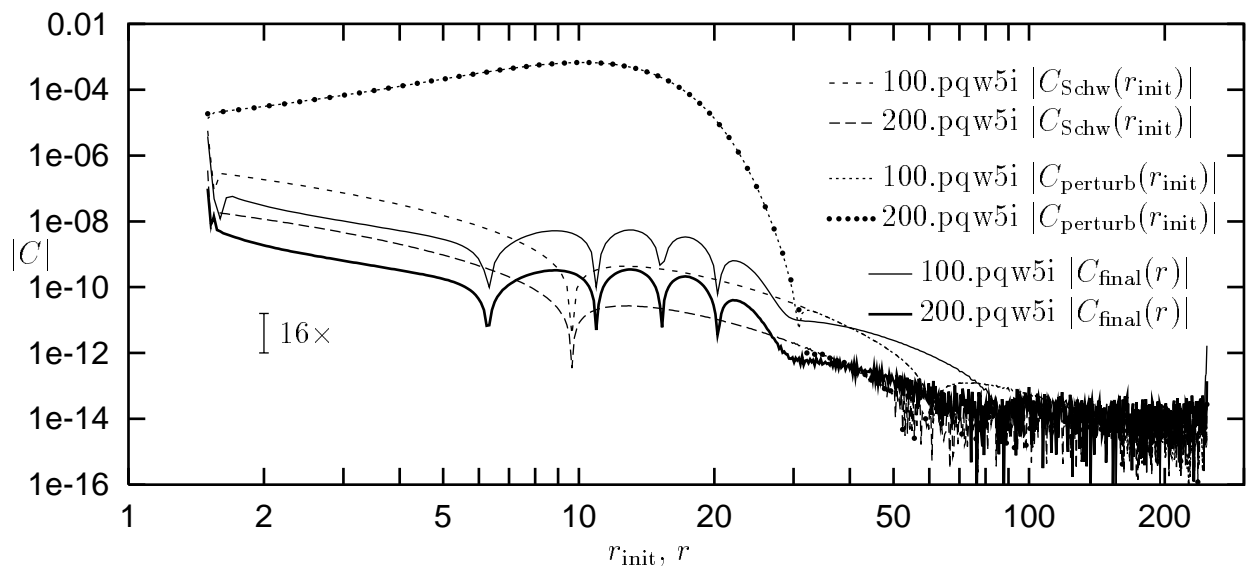
Thornburg Figure 9(b)



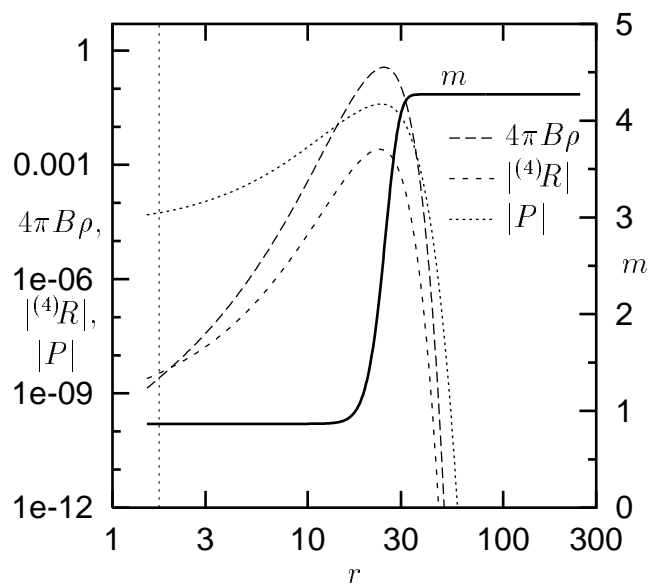
Thornburg Figure 10(a)



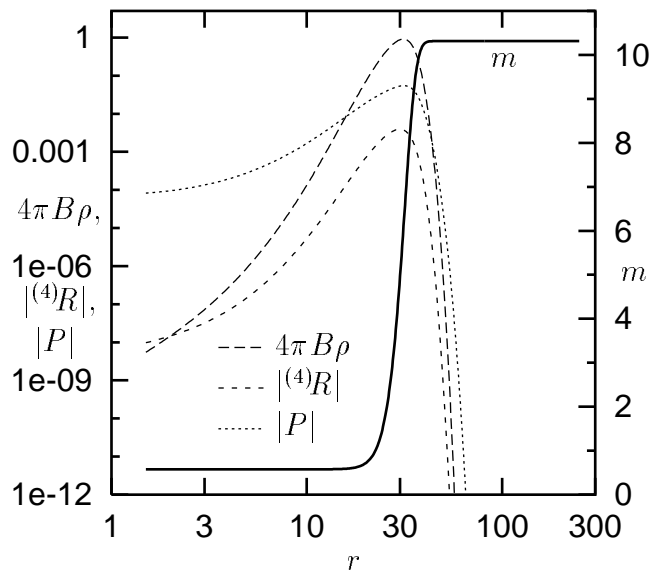
Thornburg Figure 10(b)



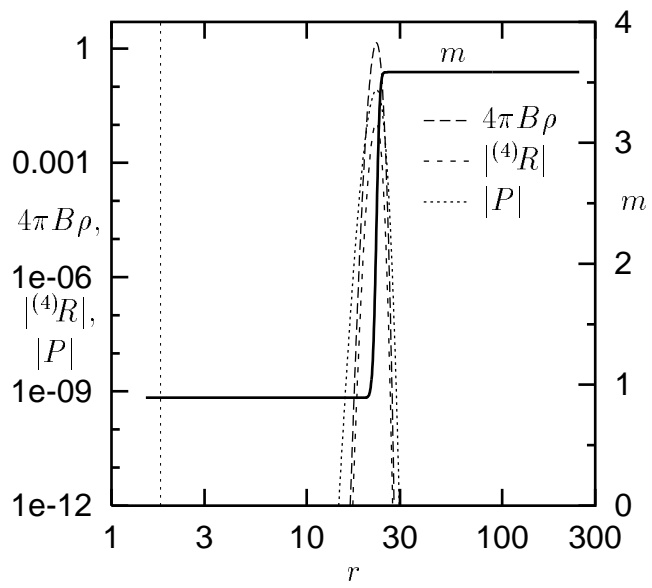
Thornburg Figure 11



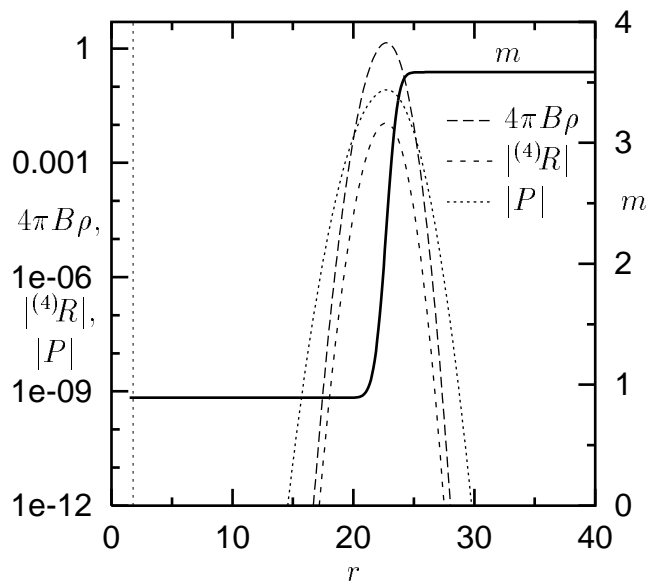
Thornburg Figure 12(a)



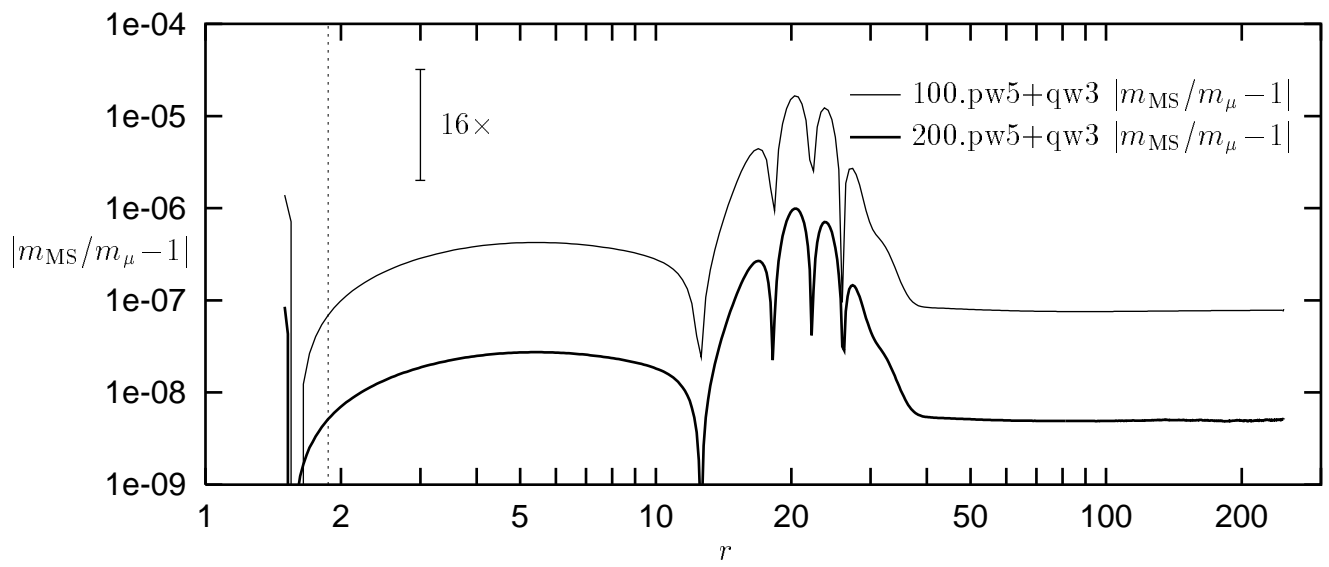
Thornburg Figure 12(b)



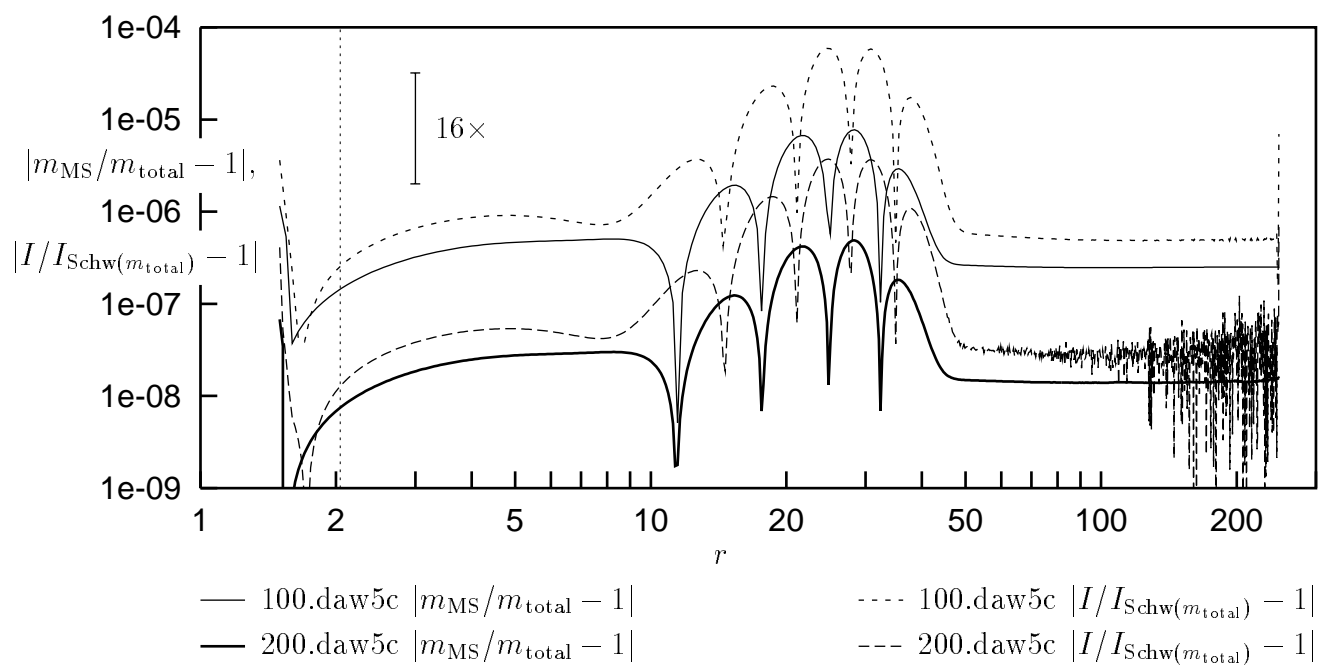
Thornburg Figure 13(a)



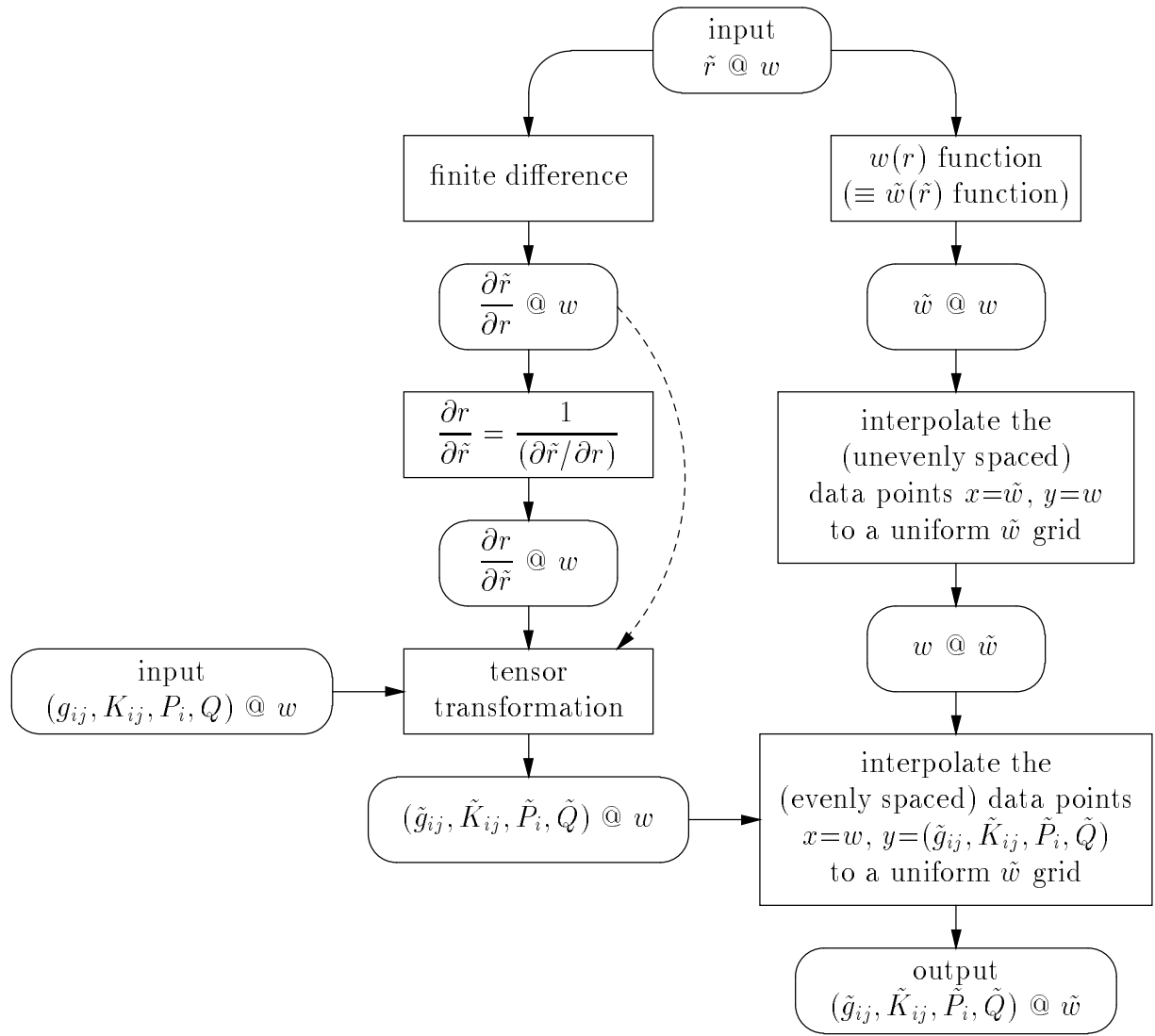
Thornburg Figure 13(b)



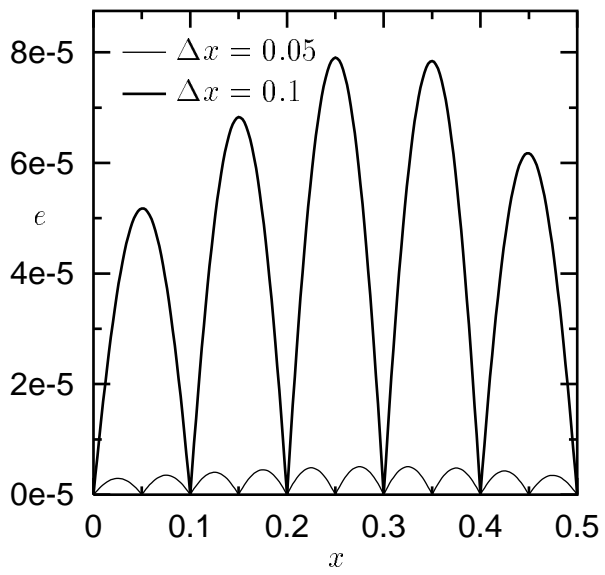
Thornburg Figure 14



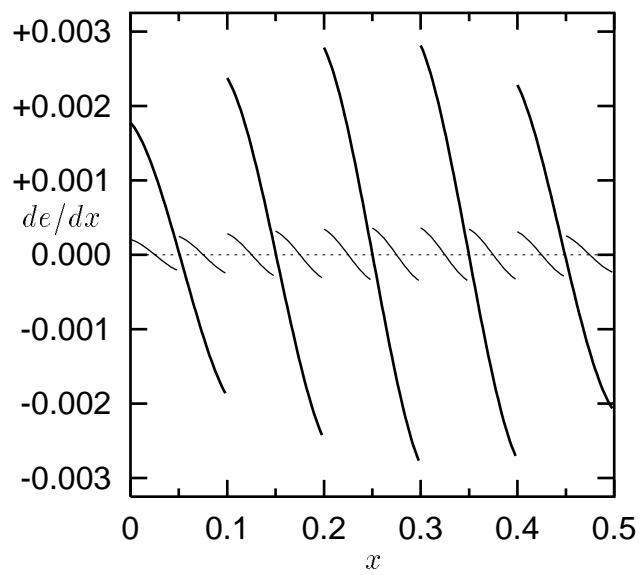
Thornburg Figure 15



Thornburg Figure 16



Thornburg Figure 17(a)



Thornburg Figure 17(b)

TABLE I. This table gives various parameters for our test initial data slices. For each slice the table shows a descriptive name, the spatial grid resolution and size, the initial perturbation (step 2 in our overall initial data algorithm of section VII), an approximate Gaussian fit to the slice’s radial scalar field density $4\pi B\rho$, the horizon’s areal radius, and a summary of the slice’s mass distribution (broken down into black hole, scalar field, and total mass).

Name	Δw	$\frac{\Delta r}{r}$ at $r=20$	w_{\max}	r_{\max}	Initial Perturbation	Approximate Profile of Scalar Field Shell ($4\pi B\rho$)	Horizon Radius	Mass		
								BH	+	SF = Total
100.pqw5	0.01	0.02	4	248	$P \rightarrow P + 0.02 \times \text{Gaussian}(r_{\text{init}}=20, \sigma=5)$	$0.0735 \times \text{Gaussian}(r=21.8, \sigma=3.5)$	1.952	0.976	+	0.641 = 1.617
200.pqw5	0.005	0.01								
100o10.pqw5	0.01	0.02								
200o10.pqw5	0.005	0.01								
100o30.pqw5	0.01	0.02								
200o30.pqw5	0.005	0.01								
100.pqw5i	0.01	0.02	4	248	$P \rightarrow P + 0.02 \times \text{Gaussian}(r_{\text{init}}=10, \sigma=5)$	$0.0205 \times \text{Gaussian}(r=12.4, \sigma=3.2)$	1.976	0.988	+	0.167 = 1.155
200.pqw5i	0.005	0.01								
100.pqw5b	0.01	0.02	4	248	$P \rightarrow P + 0.05 \times \text{Gaussian}(r_{\text{init}}=20, \sigma=5)$	$0.0365 \times \text{Gaussian}(r=24.4, \sigma=3.7)$	1.733	0.866	+	3.405 = 4.271
200.pqw5b	0.005	0.01								
100.pqw5c	0.01	0.02	4	248	$P \rightarrow P + 0.1 \times \text{Gaussian}(r_{\text{init}}=20, \sigma=5)$	$0.91 \times \text{Gaussian}(r=31.0, \sigma=4.2)$	- ^a	(0.576)	+	9.737 = 10.313
200.pqw5c	0.005	0.01								
200.pqw1	0.005	0.01	4	248	$P \rightarrow P + 0.1 \times \text{Gaussian}(r_{\text{init}}=20, \sigma=1)$	$1.42 \times \text{Gaussian}(r=22.71, \sigma=0.76)$	1.784	0.892	+	2.692 = 3.584
400.pqw1	0.0025	0.005								
100.pw5+qw3	0.01	0.02	4	248	$\left[\begin{array}{l} P \rightarrow P + 0.02 \times \text{Gaussian}(r_{\text{init}}=20, \sigma=5) \\ Q \rightarrow Q + 0.03 \times \text{Gaussian}(r_{\text{init}}=20, \sigma=3) \end{array} \right]^b$	$0.225 \times \text{Gaussian}(r=22.1, \sigma=2.5)$	1.872	0.936	+	1.666 = 2.602
200.pw5+qw3	0.005	0.01								
100.daw5c	0.01	0.02	4	248	$A \rightarrow A + 0.1 \times \text{Gaussian}(r_{\text{init}}=20, \sigma=5)$	none	2.043	1.022	-	1.022
200.daw5c	0.005	0.01								

^aAs discussed in the text in section XIE, there’s no apparent horizon within this slice’s numerical grid; the “black hole” mass shown (within parentheses) is actually the mass within the inner grid boundary.

^bThe initial perturbation is to both P and Q for this slice.